UNIVERSITY OF OKLAHOMA

GRADUATE COLLEGE

EXPLORING BEAMFORMING TECHNIQUES FOR mmWAVE SCANNING ANTENNAS

A THESIS

SUBMITTED TO THE GRADUATE FACULTY

in partial fulfillment of the requirements for the

Degree of

MASTER OF SCIENCE

By

SERGIO HIROSHI RODRÍGUEZ MASUMURA

Norman, Oklahoma

2024

EXPLORING BEAMFORMING TECHNIQUES FOR mmWAVE SCANNING ANTENNAS

A THESIS APPROVED FOR THE
SCHOOL OF ELECTRICAL AND COMPUTER ENGINEERING

BY THE COMMITTEE CONSISTING OF

Dr. Jorge L. Salazar-Cerreño, Chair

Dr. Justin Metcalf

Dr. Joseph Tischler

Acknowledgments

I want to express my gratitude to my parents Silvia Masumura and Reynaldo Rodríguez for the continuous and unwavering support that they have given me throughout the years, regardless of the distance that has separated us during my graduate studies. I dedicate all of my work to them and I want to thank them for giving me all the necessary tools to grow as a person and fulfill my goals.

I extend my appreciation to my advisor Dr. Jorge Salazar-Cerreño for his continuous guidance. Additionally, I want to thank the other members of my committee, Dr. Justin Metcalf and Dr. Joseph Tischler, for their support and commitment.

I would like to thank the Advanced Radar Research Center (ARRC) for their research support, as well as its members for allowing me to grow and learn with them. Thank you for helping me become a better engineer and a better researcher alongside them, giving me feedback and teaching me lessons. In particular, I would like to thank Mariel Avalos, Felipe Moncada, Marcelo Moreno, Alexis Oblitas, Syed Jehangir, Khuda Burdi, Elizabeth Joyce, Jorge Alva and César Salazar.

Finally, I would like to express my deepest gratitude to my partner Majd Haddad for her unconditional support. Thank you for believing in me during this journey, for encouraging me to keep going forward, for helping me even when you did not have to, and most importantly, for always being by my side when I need you the most.

Abstract

Radar and communication systems greatly benefit from having a highly directive antenna, with a narrow beamwidth. Previous studies have been performed on multiple techniques to obtain a reduced beamwidth, and the aim of this present work will be placed on exploring two of them. The first one is dielectric lenses, which consists of a dielectric structure placed outside of the antenna, which collimates the trasmitted radiation forward, as a planar wave. The second technique is virtual arrays, which allows a radiation pattern with a reduced beamwidth to be obtained by modifying the spacing between the elements in the transmission and reception arrays.

Work on dielectric lenses has been widely reported, ranging from the use of metamaterials that allow to achieve a dielectric constant close to zero, to the use of additive manufacturing with artificially engineered dielectrics to achieve the desired beamwidth reduction. However, a clear procedure to design lenses based on certain radiation parameters has not been explored yet.

Furthermore, research performed on the optimization of antenna elements in arrays to reduce the beamwidth has also been done. Multiple techniques such as numerical optimizations and compressive sensing have been used, and a reduction between 20% and 40% have been obtained. Nonetheless, these techniques do not account for electronical beam steering, which is a main feature of antenna arrays.

With that in mind, the objective of this thesis is to develop a methodical design procedure for both dielectric lenses and virtual arrays. In the case of lenses, the aim is to derive

equations that allow for estimating their size and obtain a dielectric constant profile regardless of the desired shape. As for the virtual arrays they are explored in order to obtain the minimum achievable beamwidth with a certain number of elements, without compromising both the beam steering capabilities and amplitude tapering.

Table of Contents

Acknowledgment **iv**

Abstract **v**

Table of Contents **vii**

List of Figures **x**

List of Figures **x**

1 Introduction **1**

1.1 Motivation 1

1.2 Literature Review 2

1.2.1 Dielectric Lenses background 2

1.2.2 Virtual Arrays background 4

1.3 Proposed Work 6

1.3.1 Dielectric Lenses 6

1.3.2 Virtual Arrays 7

1.4 Thesis Outline 8

2 Fundamentals **10**

2.1 Radiation Pattern 10

2.2 Directivity and Gain . . . 11
2.3 Beamwidth . . . 13
2.4 Phase Center . . . 14
2.5 Antenna Arrays . . . 15
2.6 Refraction theory . . . 18
2.7 Summary . . . 20

3 Design Procedure and Tradeoffs 22

3.1 Dielectric Lenses . . . 22
3.1.1 Dimensions . . . 22
3.1.2 Focal Point and Sidelobes . . . 23
3.1.3 Dielectric Constant Profile . . . 24
3.1.4 Quantization errors . . . 28
3.1.5 Unit Cells . . . 29
3.1.6 Tradeoffs . . . 31
3.2 Virtual Arrays . . . 33
3.2.1 Number of Virtual Elements . . . 33
3.2.2 Grating Lobes and Scanning . . . 38
3.2.3 Taylor Tapering . . . 39
3.2.4 Tradeoff analysis . . . 42
3.3 Summary . . . 44

4 Results 46

4.1 S-band dielectric lens design and simulation . . . 46
4.2 S-band dielectric lens implementation . . . 53
4.3 Virtual Array design and simulation . . . 56
4.4 Virtual Array implementation . . . 59

4.5 Summary 72

5 Epilogue **74**

5.1 Conclusion 74

5.2 Future Work 76

References **78**

List of Figures

2.1 Radiation pattern of an antenna system in polar coordinates. The main beam, sidelobes and backlobe radiation are also indicated. 11

2.2 Radiation pattern (red) and analog isotropic radiation pattern (green) to explain the concept of directivity. 12

2.3 Half-power beamwdith (red) and First-null beamwidth (blue) of a radiation pattern, indicated as the angle located between the -3 dB points of the main lobe, and the nulls of the main lobe, respectively. 13

2.4 Horn antenna with its phase center, indicated as the red point with spherical waves radiating out of it, and its source excitation, indicated as a vertical arrow. 15

2.5 Comparison between (a) one single radiating element and (b) a linear array of 6 elements. The red lobes represent the main beam of the respective radiation patterns. Each element is fed by its own sinusoidal source. 16

2.6 MATLAB simulations of the normalized radiation patterns of two arrays with a spacing of half wavelength and uniform amplitudes for (a) 4 elements and (b) 20 elements. 17

2.7 MATLAB simulations of the normalized radiation patterns of two arrays with 8 elements and uniform amplitudes for (a) spacing of half wavelength and (b) spacing of two wavelengths. 17

2.8 MATLAB simulations of the normalized radiation patterns of two arrays with 8 elements and a spacing of half wavelength for (a) uniform amplitudes and (b) amplitudes with Taylor tapering. 17
2.9 Refraction of a ray of light (red arrow), going from Medium 1 to Medium 2. Each medium has a different index of refraction. 19
2.10 Schematic of rays of light going through (a) convex and (b) concave lenses. 19

3.1 Geometry showing the relationship between the desired illumination of the lens (given by the angle θ_{3s}, which stands for the 3 dB beamwidth of the source) and the focal point (FP). D is the diameter of the lens, and t is its thickness. 23
3.2 Discretized dielectric constant profile across the concentric rings of a flat lens. The blue line in the plot represents the desired profile, and the black line represents the different steps taken in the lens. The vertical axis is the dielectric constant (ε_r),the horizontal axis is the radial distance in the lens (d), and t is the lens thickness. 24
3.3 Geometry showing the variables used to calculate the lens profile. FP is the focal point, d_n is the distance between the source and the nth concentric ring, and Δx is the distance between said ring and the center of the lens. . . 25
3.4 Schematic of an example of a conformal lens with different values of thickness. The focal point (FP), variable thickness (t_n) and phase shift of air (ϕ_{Air}) are indicated. 27
3.5 Assembly of Hexagonal Unit Cells into a large, periodical structure. R is the radius of the hole, s is the side of the hexagon and t is the thickness of the unit cell. 30

3.6 Top view of an assembled lens. The different shades of gray represent different values of dielectric constant. D is the diameter of the lens. 31
3.7 Comparison between the required dielectric constant profiles of two lenses with different values of thickness. 32
3.8 Comparison between the required dielectric constant profiles of two lenses with different values of focal point. 32
3.9 Visual demonstration of the synthesis of a virtual array applying the concept of convolution for (a) half-wavelength spacing between elements in both arrays and (b) modifying the spacing in reception to 1.5 wavelengths. In both cases, one array moves with respect to the other, and the virtual array is the resulting overlap between them. 37
3.10 Comparison of the normalized two-way patterns of two 4-element arrays (Tx and Rx) with a spacing of half-wavelength (0.5λ) and two-wavelength (2λ) in reception. 38
3.11 Beam steering capabilities of two 4-element arrays (Tx and Rx), applying the virtual array concept. 39
3.12 Grating lobe periodicity for a 4-element array with two-wavelength (2λ) spacing for uniform distribution and -30 dB Taylor. While the nulls are not in the same angular positions, the grating lobes are. 40
3.13 Taylor distributions (-15 dB, -20 dB, -25 dB and -30 dB) applied to the amplitudes of the reception array, maintaining the virtual array concept (4-element arrays in Tx and Rx). 41
3.14 Beam steering capabilities of two 4-element arrays (Tx and Rx), with a -20 dB Taylor tapering in reception, maintaining the virtual array concept. . 41

3.15 Comparison of the two-way pattern's broadside beamwidth of two arrays when changing their number of elements, for common half-wavelength spacing and for this technique. 43
3.16 Difference of the two-way pattern's broadside beamwidth of two arrays when changing their number of elements, in degrees (left axis) and percentage (right axis) 43

4.1 FormLabs additive manufacturing equipment. Form3 3D printer (left), Isopropil alcohol cleaner (center) and UV light curing device (right). 47
4.2 Material characterization setup and its components at the mmWave and sub-terahertz lab. in the Radar Innovations Laboratory. 47
4.3 Small sample of Grey V4 resin to be printed for characterization of the material. 48
4.4 Dielectric constant (y axis) vs frequency (x axis) plot of the Grey V4 resin sample, in the Keysight Material Measurement Suite software. The average measured value for the test sample is 2.7. 48
4.5 Dielectric constant profile of the S-band flat lens. 50
4.6 Final design of the S-band dielectric lens. The different colors represent different values of dielectric constant. 51
4.7 Simulation setup of the lens and the source in Ansys HFSS, with the respective focal point (FP) and diameter (D) indicated. 52
4.8 Simulated radiation patterns of the (a) E-plane and (b) H-plane of the source with and without the lens. 52
4.9 Model of one quarter of the lens in PreForm. 53
4.10 Fabricated (a) quarter of the lens and (b) fully assembled lens. 54
4.11 (a) Model and (b) fabricated frame for the antenna source and the lens. . . . 54

4.12 Setup of the Antenna Under Test (AUT) with the lens inside of the far-field anechoic chamber. 55
4.13 Measured radiation patterns of the (a) E-plane and (b) H-plane of the source with and without the lens. 55
4.14 Ansys HFSS individual radiation pattern of the antenna element used in the arrays. 56
4.15 Schematic of the (a) transmission and (b) reception arrays simulated in Ansys HFSS. The highlighted antennas are excited, while the rest are just passive elements. 57
4.16 Ansys HFSS results of the Virtual Array system for uniform distribution (top left), 30 dB Taylor in the reception array (top right), and beam steering at 20° (bottom left) and 50° (bottom right) with a 20 dB Taylor distribution in the reception array. 58
4.17 Steps for designing a series-feed linear array. (a) A single patch antenna's length and width are tuned to obtain a purely real input impedance at the desired frequency. (b) 50 ohm transmission lines are added at each side of the patch, with a total horizontal length of half-wavelength (or the desired spacing between elements). Mitered bends are added, and their length is tuned to obtain a 360° difference between both ports at the edges of the transmission lines. (c) Multiple elements from step b are assembled together, and a 50 ohm transmission line is added at the beginning of the array. The length of this transmission line is tuned to obtain a purely real input impedance. (d) A quarter-wave transformer is added to convert the input impedance from panel b into 50 ohms. One last 50 ohm transmission line is added after this transformer. 60

4.18 Simulated radiation pattern of the series-feed patch antenna array with half-wavelength spacing. 61
4.19 Simulated radiation pattern of the series-feed patch antenna array with two-wavelength spacing. 61
4.20 Picture of the Rogers 4350B substrate inside of the LPKF ProtoLaser machine. The board has been taped to the surface to secure it during the fabrication process. 62
4.21 Fabricated antenna arrays with half-wavelength spacing. Three arrays were fabricated (labeled 1, 2 and 3) and the one with the best performance was selected. 63
4.22 Fabricated antenna array with two-wavelength spacing. Only one array was fabricated due to time and lack of material constraints. 63
4.23 Fabricated antenna in the near-field anechoic chamber, with a Rohacell foam support and an NSI-RF-WR90 probe. 64
4.24 Measured azimuth radiation pattern of the transmission antenna array with a half-wavelength spacing. The data is truncated at $\pm 70^{\circ}$ due to the maximum scan window in the chamber and the NSI 2000 software (5'x5'). . . . 64
4.25 Measured azimuth radiation pattern of the reception antenna array with two-wavelength spacing. The data is truncated at $\pm 70^{\circ}$ due to the maximum scan window in the chamber and the NSI 2000 software (5'x5'). . . . 65
4.26 Two-way azimuth pattern of the transmission (Tx) and reception (Rx) arrays, calculated and plotted as the overlap between both patterns. 65

4.27 Setup to calculate the processed radiation patterns in elevation for (a) half-wavelength spacing and (b) two-wavelength spacing. The azimuth radiation patterns shown were measured for one array alongside the green dashed line axis, whereas the red dashed line indicates that the patterns need to be computed across this axis. 66
4.28 Measured elevation radiation pattern of the (a) transmission antenna array with a half-wavelength spacing, and the (b) reception antenna array with two-wavelength spacing. 66
4.29 Radiation pattern of the equivalent elevation transmission 4-element array with half-wavelength spacing. 67
4.30 Radiation pattern of the equivalent elevation reception 4-element array with two-wavelength spacing. 67
4.31 Radiation pattern of the equivalent elevation two-way system consisting of transmission (Tx) and reception (Rx). 67
4.32 Beam steering capabilities of the equivalent elevation two-way system. . . . 68
4.33 Taylor distributions (-15 dB, -20 dB, -25 dB and -30 dB) applied to the amplitudes of the reception array, for the equivalent elevation two-way system. 68
4.34 Beam steering capabilities of the equivalent elevation two-way system, with a -20 dB Taylor tapering in reception. 69
4.35 16x1 S-band patch antenna array placed in the near-field anechoic chamber for measurements. 70
4.36 Setup of the 16x1 S-band antenna array, where the highlighted elements are the only ones that were excited for measuring (a) transmission with a spacing of half-wavelength and (b) reception with a spacing of two wavelengths. 70

4.37 Measured results of the two-way system by using the S-band antenna array with two configurations for transmission and reception. The plots show uniform distribution (top left), 20 dB Taylor in the reception array (top right), beam steering at 30° (bottom left), and both beam steering (30°) and Taylor tapering (-20 dB) in the reception array (bottom right). 71

Chapter 1

Introduction

1.1 Motivation

Modern radar and communication systems utilize phased-array antenna technologies, benefiting from their agility in beam steering, fast temporal resolution, and diverse multi-function capabilities. In microwave frequencies, the implementation of electronic phased-array radar or communication systems is feasible, thanks to the availability of commercial microwave components. However, in the case of mm-Wave bands, handling a high number of elements presents its own set of challenges, including complexity, power density, and cost of active components [1–5], which demand the use of techniques that can achieve similar performance without compromising affordability. It is shown by Balanis [6] that arrays with a large number of elements are required to obtain a narrow beamwidth, which is a feature that can be benefitial for both radars [7] and communication systems [8, 9]. Out of the multiple solutions that have been developed to overcome this, two of them show great promise in the present due to the current manufacturing opportunities and cost constraints: dielectric lenses and virtual arrays. Firstly, lenses have been explored as a structure placed in front of the antenna to make it more directive and reduce its beamwidth, and they are gaining popularity in the present given that they can be produced with additive manufacturing and affordable 3D printers. This results in a precise, reliable and inexpensive solution,

and a wide variety of research has been performed on them, ranging from fabricating them with mixed materials to using metasurfaces. Virtual arrays, on the other hand, enable the use of fewer antenna elements to obtain a pattern that would otherwise require a greater number of them [10–12], effectively reducing the cost of systems due to the fewer required active elements. This technique, however, has not been too explored in the literature in comparison with other mathematical optimization methods. In addition, there are no clear procedures and scanning antenna performance provided in the literature for both techniques in order to improve beamwidth, minimize sidelobes and destroy grating lobes. My present work aims to develop and test a methodical series of steps and equations to properly apply each technique, and support them with simulated and measured results.

1.2 Literature Review

The following section aims to assess the work done in the literature for both dielectric lenses and virtual arrays, emphasizing on the identified achievements and limitations of each one.

1.2.1 Dielectric Lenses background

A wide range of research has been performed to improve the beamwidth of antenna systems, including different techniques to modify the system architecture or adding extra components such as lenses. Work regarding dielectric or metamaterial-based lens have been used and reported in the literature to reduce the phase error and improve the radiation performance of horn antennas. Ramaccia *et al.* [13] designed a flat lens by using a conventional dielectric alongside a metamaterial that allows obtaining a really low dielectric constant (close to zero). This allows the horn antenna in which the lens is being used to have an improved performance across a wide range of frequencies in C-band. Chen and

Ge [14] applied a metasurface lens in the aperture of a horn antenna with the purpose of manipulating the transmitted profile of amplitudes and phases. This was performed to reduce the sidelobe level and the backlobe level of the radiation pattern. Mustafa *et al.* [15] designed and simulated a gradient index dielectric lens for a horn antenna by aiming to correct the phase error in its aperture. This allowed to obtain a shorter antenna than conventional ones. The lens was built as a dielectric cylinder that was radially and periodically perforated with different radii to compensate the phase differences, and a high directivity of 26.4 dBi was achieved with it. Bauerle *et al.* [16] designed and implemented a lightweight dielectric lens for a quad-ridge horn antenna to improve its aperture efficiency to about 70% across its frequency band of operation from 5 to 15 GHz. Turk and Keskin [17] applied a dielectric lens as a partial dielectric loading of a ridged horn antenna. It was located inward towards the aperture of the antenna, but not covering the whole transversal area (positioned between the ridges). This loading was added to the antenna in order to enhance its gain by 5 dB across the 5 to 15 GHz band, and correct the pattern distortion in its higher operational frequencies.

Additionally, 3D-printed planar GRIN lens antennas in particular have also been used before to help reduce the beamwidth of antennas. McManus *et al.* [18] presented a theoretical and simulated comparison between flat and profiled dielectric lenses. Equations for obtaining the profile for each case were provided, but their derivations were not. Zhang *et al.* [19] designed and fabricated a 3D printed flat dielectric lens, using concentrical rings with different permittivities, ranging from 1.30 to 2.72, to improve the gain of an antenna. The permittivity values were obtained by modifying an internal air void volume in each ring and applying the Nicholson-Ross-Weir method. They also designed a second lens with the same qualities as the first one, in which the thickness was greatly reduced by half, and this was done by enhancing the dielectric properties of the lens using metallic patches between the rings. Poyanco *et al.* [20] designed and fabricated a wideband 3D printed flat lens with

different concentric dielectric constants that were achieved by using ABS filaments with high permittivity values and modifying the infill percentages for each ring. Additionally, Zhang *et al.* [21] also designed a 3D printed lens that applies different infill percentages to vary the effective permittivity across multiple concentric rings. However, another approach that they considered was applying artificially engineered dielectrics by combining different dielectric constants per unit cell of regular ABS ($\varepsilon_r = 2.7$) and a high permittivity fillament called PREMIX PREPERM ($\varepsilon_r = 4.4$), with an addition of metallic patches between them. The results showed a great improvement in the gain by 8.7 to 15.6 dB, and an good efficiency of 82% over a frequency range of 12 to 40 GHz. Imbert *et al.* [22] worked on fabrication and measurement of a flat dielectric lens that not only improves the antenna gain, but also allows to have beam steering by slightly changing the position of the source.

1.2.2 Virtual Arrays background

Furthermore, considering the aforementioned constraints found in high frequencies, multiple different techniques have been implemented in antenna arrays to modify the shape of the pattern transmitted by the antennas and obtain narrower main beams without the need to use too many elements. Liu *et al.* [23] proposed a mathematical method to calculate the minimum required number of antenna elements to produce a desired pattern by performing singular value decomposition. They then applied the matrix pencil method to synthesize the necessary excitations and positions to achieve said pattern. The mathematical procedure is very rigorous and allows for a reduction of elements of more than 40%, but it does not account for beam steering. Shen and Wang [24] proposed a method with matrix transformations that enhances the matrix pencil method, and also allows to calculate the positions and excitations of fewer antenna elements (20% to 40% reduction). This method particularly specializes in the synthesis of large arrays. Kikuchi *et al.* [25] applied a signal

processing technique called compressive sensing to reduce the number of elements in a phased array weather radar and reconstruct the received signals to a very similar state as the one that would otherwise be collected by a higher number of antennas. They performed simulations and processed some measured data, showing a good feasibility in the use of this technique for a reduction in the components. A reduction factor of 75% was achieved (going from 128 to 96 elements). Zhang *et al.* [26] performed numerical optimizations to the calculations of position and excitation of antenna elements to obtain very similar patterns to the ones generated by the Chebyshev and Taylor-Kaiser distributions described by Balanis [6]. The new obtained patterns are the result of arrays with a lesser number of elements (30% and 38% fewer elements, respective to the aforementioned distributions), therefore achieving a good level of optimization and improvement from conventional arrays. Dorrah and Eleftheriades [27] proposed a new type of phased array that positions its antenna elements on the periphery of a circular cavity. This circular cavity would have slots on the top that radiate a pencil beam pattern that can be steered by modifying the phases of the excitations. These different presented techniques, however, either do not show a great reduction in the number of antenna elements, or present fixed patterns with limitations when it comes to electronic beam steering capabilities, i.e., they do not present patterns steering out of broadside, or they only achieve it with certain scanning angles. This last concept of steering is another really important aspect of these antenna systems. The idea of phased-arrays has been implemented to electronically steer the main beam of the radiation pattern to a different angle by modifying the excitation phases of each element [28]. Work has been performed to apply this concept in communications [29–31] and radars [32, 33], and other different approaches have also been considered to achieve this feature such as frequency scanning [34], reactive loading [35], antenna beam superposition [36], and metasurfaces [37]. The main problems that they face are either low (or fixed) scanning angles or the apparition of undesired grating lobes in the pattern.

The present work proposes two techniques that overcome all these obstacles and allow for obtaining a narrow beamwidth. In contrast with previous research, a methodical procedure is established to appropriately take advantage of these techniques without obtaining a rigid solution.

1.3 Proposed Work

In the proposed research, two state of the art methods for beamwidth reduction in antenna systems are explored, discussed, delved into, implemented and tested. The first method is dielectric lenses, which was selected due to their potential fabrication using additive manufacturing, which results in a cheap but effective solution. The second method is called virtual arrays, and it was explored due to its novelty and the current lack of depth and procedures in the literature. Both methods are discussed in detail in the following two subsections.

1.3.1 Dielectric Lenses

Firstly, the design of a gradient index (GRIN) flat dielectric lens is proposed. This type of lens has applications that widely range from highly directive antennas for the navy, to millimeter-wave antennas for material characterization. This type of lens is a flat cylinder made of dielectric, with a changing permittivity across concentric rings that will reduce the beamwidth of an antenna. This changing permittivity modifies the phase of the wavefront emitted by the antenna, aiming to convert it into planar waves that are focused in the desired direction. This is implemented with the application of artificial dielectric layers in hexagonal unit cells that are assembled together. The basic lens dimensions are calculated to obtain the desired beamwidth by approximating the lens as a radiating aperture antenna, whereas the necessary dielectric constant gradient index profile is obtained by performing

an analysis of the phase of the transmitted signal across the surface of the lens. A new equation to calculate the dielectric constant profile is derived for fabricating lenses, which differs from the ones in the literature due to its potential to also work for lenses with different values of thickness, allowing the creation of conformal lenses or even lenses with a simultaneous change in curvature and dielectric constant. The resin for the lens fabrication was tested in a material characterization setup in order to determine its value of dielectric constant. An S-band lens was designed and simulated with that material using the Ansys HFSS software, aiming to verify the formulated math procedure. This lens was then split into four parts, as it was too big for the 3D printer in order to be fabricated using additive manufacturing, and then assembled together using epoxy glue. A frame was constructed to hold the lens in place at the required distance from the source. This setup was then tested in a far-field anechoic chamber. The results show good agreement between the theory, the simulations and the measurements, indicating that the developed procedure works appropriately.

1.3.2 Virtual Arrays

Virtual Arrays are also analyzed as a technique that allows for beamwidth reduction in an antenna system by only modifying the position of the antenna elements. It is currently being used in small systems such as automotive radars, but it has not been too explored in the literature. This concept starts by considering that every system has transmitter elements and receiver elements, thus there are two radiation patterns that combine into one overall two-way pattern. The present work explores virtual arrays as a technique to carefully place the nulls and peaks in the two patterns to avoid grating lobes, presenting multiple guidelines to obtain the narrowest achievable beamwidth, while also maintaining electronic beam steering capabilities. Taylor amplitude tapering is also examined and applied to reduce the

sidelobe level of the obtained radiation pattern. These novel guidelines help to design systems that can overcome the common limitations of the current optimization methods, which are very limited when we do not use them to scan in broadside. An antenna array system with 4 transmission elements and 4 reception elements was optimized and simulated in Ansys HFSS in order to verify this concept, showing great agreement with the theoretical patterns. Additionally, two 4-element series-feed X-band linear antenna arrays were designed and fabricated using a Rogers 4350B substrate in an LPKF ProtoLaser machine. These arrays were designed with different optimized values of element spacing and were individually tested in a near-field anechoic chamber. Their far-field patterns were computed using a near-field to far-field transformation, and the obtained results show that the virtual arrays concept works. Furthermore, the measured elevation patterns of each array were taken and processed to obtain the patterns of a larger steerable array, which verify the robustness of the implemented procedure when it comes to scanning and amplitude tapering. Lastly, an S-band 16x1 antenna array was used due to having its own TR module with phase shifters and attenuators for each element, in order to measure real two-way patterns with amplitude tapering and beam steering out of broadside.

1.4 Thesis Outline

This thesis presents a comprehensive study of multiple state-of-the-art beamforming techniques for antennas in 5 chapters. Chapter 2 explains some basic concepts that are needed to understand the developed procedures, such as antenna fundamentals and refraction theory. In chapter 3, two state-of-the-art beamforming techniques are presented: dielectric lenses and virtual arrays. The design procedures for both cases are introduced, including a step by step explanation of how to appropriately apply each technique, including and analyzing all the necessary equations. Tradeoffs of each technique are discussed,

particularly emphasizing on when to use each one of them. Chapter 4 presents the simulated and measured results, showing the improvements in the antenna beamwidth and comparing them with the theoretical results. Lastly, chapter 5 concludes the thesis by discussing the implications of the research and the significance of the discussed methods for current radars and communication systems.

Chapter 2

Fundamentals

In this chapter, fundamentals about antenna systems are given, focusing on the measurable parameters of antenna patterns and the concepts of antenna arrays, emphasizing on linear arrays and the variables that can be modified in them to achieve different radiation patterns. These concepts are essential for explaining the purpose of the beamwidth reduction techniques that will be discussed in next chapter. Additionally, basic refraction theory is considered in order to explain the main concepts for lens fabrication, as well as giving the relation between index of refraction (for optical lenses) and dielectric constant (for microwave lenses).

2.1 Radiation Pattern

Ideally, antenna systems would only radiate electromagnetic waves into the desired direction(s), such as a TV parabolic dish only pointing to its respective satellite, or a cellphone tower radiating equally towards all directions. In reality, antennas and antenna arrays are complex structures that can direct the energy into certain directions, but they also have some leakage in other angles. The radiation pattern is a way to represent the power distribution as a mathematical graph in function of the space coordinates [6]. Figure 2.1 shows an example of a radiation pattern in polar coordinates. Commonly, the power in the pattern

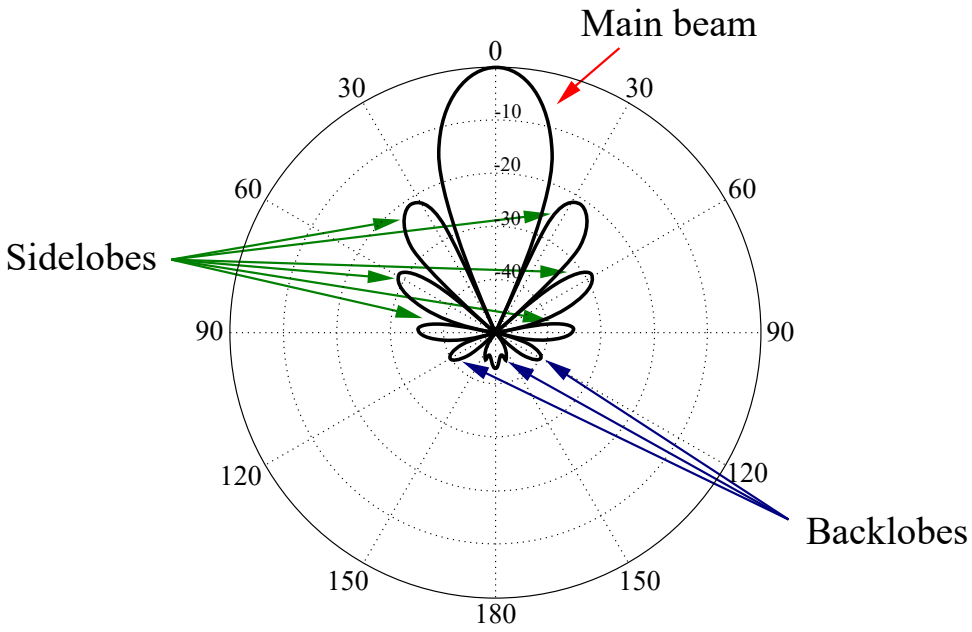

Figure 2.1: Radiation pattern of an antenna system in polar coordinates. The main beam, sidelobes and backlobe radiation are also indicated.

is logarithmically scaled in dB, and the one illustrated in the aforementioned Figure is also normalized with respect to its maximum power (the maximum point of the pattern is at 0 dB). This image also shows the different lobes that usually appear, which are bounded by regions of relatively weak radiation intensity, also called "nulls". Additionally, a common measurement of these lobes is called the Sidelobe Level, which defines how much energy is going into the sidelobes with respect to the highest point of the main beam.

2.2 Directivity and Gain

Antennas are frequently characterized by their directivity and/or gain, which are terms that are commonly mistaken as synonyms. Firstly, according to the International Electrotechnical Commission (IEC), directivity can be defined as a ratio between the radiation intensity in any given direction with respect to the average radiation intensity over all directions [6]. This definition is expressed in Equation 2.1, where D is the directivity, U is

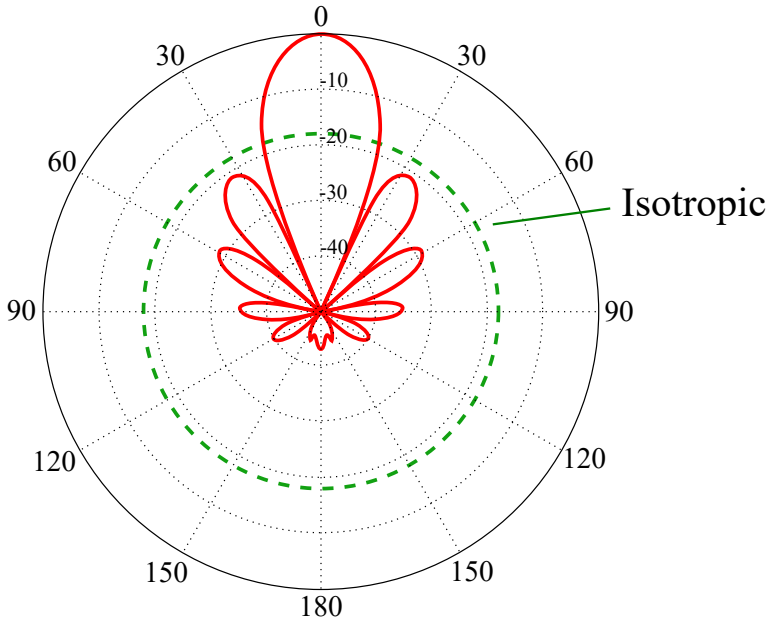

Figure 2.2: Radiation pattern (red) and analog isotropic radiation pattern (green) to explain the concept of directivity.

the radiation in the desired direction (it is assumed to be the maximum radiation intensity if not specified), and U_0 is the average radiation intensity.

$$D = \frac{U}{U_0} \tag{2.1}$$

Additionally, Figure 2.2 shows a visual representation of antenna directivity, where the green dashed circle is the pattern of an analog antenna with the same average radiation intensity across all directions, also called an isotropic source. The directivity in any direction would be the ratio between the red (actual radiation pattern) and the green plots. Now, the concept of gain is closely related to directivity, but it is a measurement that also accounts for the efficiency of the antenna, i.e. its losses across all directions. This can be reflected on Equation 2.2, where $G(\theta, \phi)$ is the gain, and e_{cd} is the antenna radiation efficiency.

$$G(\theta, \phi) = e_{cd} D(\theta, \phi) \tag{2.2}$$

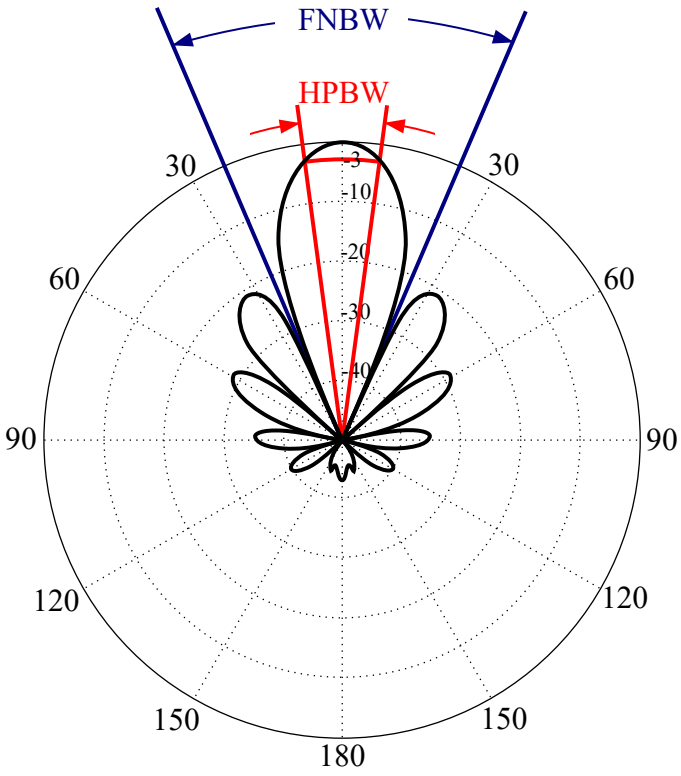

Figure 2.3: Half-power beamwdith (red) and First-null beamwidth (blue) of a radiation pattern, indicated as the angle located between the -3 dB points of the main lobe, and the nulls of the main lobe, respectively.

2.3 Beamwidth

Balanis [6] describes the beamwidth of an antenna as the angular separation between two points on opposite sides of the pattern maximum. It is a measure of how narrow or wide the mainbeam of the pattern is, and it is commonly inversely proportional to how directive the antenna is. The most common ones are the Half-power beamwidth (HPBW), which measures the angular width at the points in which the maximum power drops by half, or -3 dB in logarithmic scale, and the First-null beamwidth (FNBW), which measures it at the nulls between the main beam and the subsequent sidelobes. An example of the HPBW and the FNBW of a pattern is indicated in Figure 2.3. Additionally, some approximations

are given to calculate the beamwidth of different types of antennas [6], and the ones that are the most relevant for this work are shown in Equations 2.3 and 2.4, for a uniform line-source or linear antenna array, respectively, where l is the length of the antenna, and λ is the wavelength.

$$HPBW_{degrees} = \frac{50.6}{(l/\lambda)} \tag{2.3}$$

$$FNBW_{degrees} = \frac{114.6}{(l/\lambda)} \tag{2.4}$$

2.4 Phase Center

According to the IEEE APS Standards [38], the phase center of an antenna can be defined as a reference point in which the radiation of electromagnetic waves spreads outwards in a spherical fashion. This means that the phases of the waves are (approximately) the same across all points of the sphere, almost as if they were radiating from the phase center. Since antennas are real-life structures and not the same as a theoretical single point that radiates, we utilize its phase center as an equivalent source for positioning other components with respect to the antenna, such as lenses or reflectors. Figure 2.4 shows a phase center as an equivalent point source of an antenna.

An experimental method to obtain the phase center of a horn antenna is presented by Plaza *et al.* [39], where the unwrapped values of phase in near-field measurements are required. In my present work, however, the phase center was estimated in simulations of the horn antenna by analyzing phase front profiles across the direction of propagation.

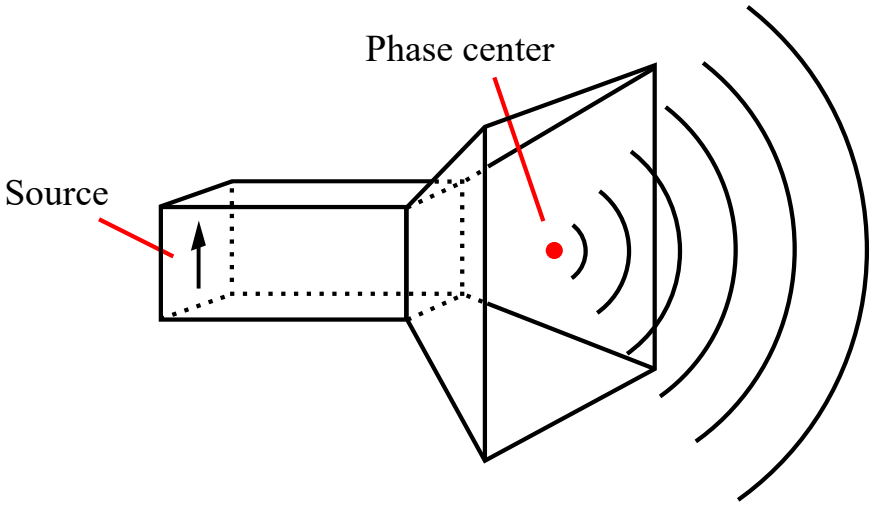

Figure 2.4: Horn antenna with its phase center, indicated as the red point with spherical waves radiating out of it, and its source excitation, indicated as a vertical arrow.

2.5 Antenna Arrays

The concept of directivity that was explained before is very important for multiple applications. According to Balanis [6], the required tradeoff to obtain an increase in directivity is a larger electrical size of the antenna. This is commonly performed by creating an *array*, which is an ensemble of radiating elements that effectively creates a larger antenna, without necessarily increasing the size of each individual element. There are multiple possible array configurations, such as linear, rectangular or circular, and each one of them comes with its advantages and disadvantages, but the present work will focus on linear arrays. Figure 2.5 shows an illustration of a linear array in comparison to a single antenna element, showing how having a larger effective antenna size generates a higher directivity. Additionally, it is important to notice how the beamwidth narrows as the directivity increases, effectively showing how the energy is being focused on one direction. Despite being the simplest form of antenna arrays, there are multiple parameters that can be modified in linear arrays to obtain different performances in the radiation pattern, such as the

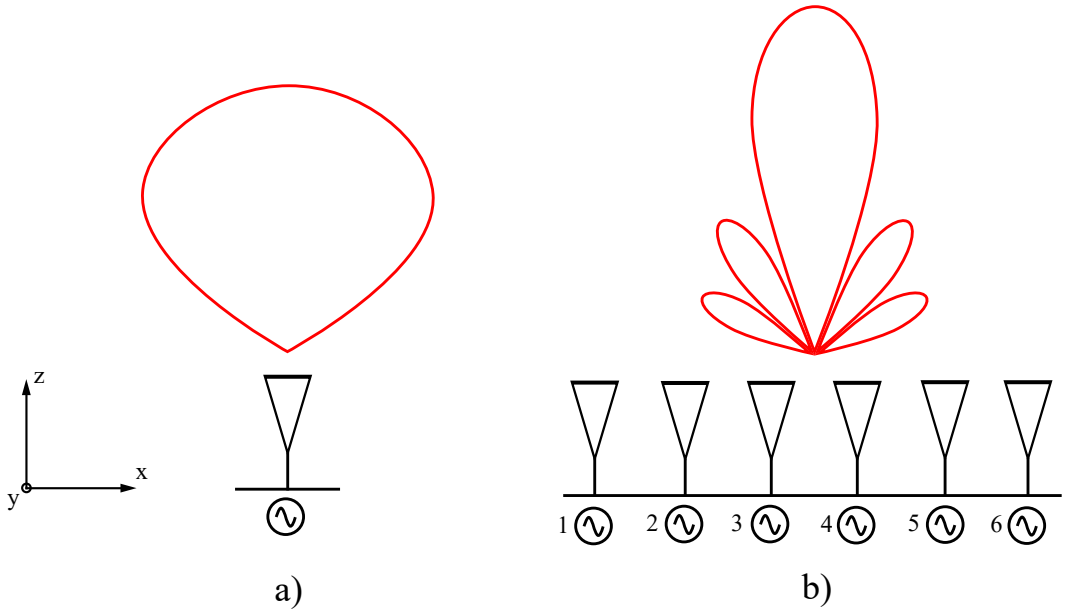

Figure 2.5: Comparison between (a) one single radiating element and (b) a linear array of 6 elements. The red lobes represent the main beam of the respective radiation patterns. Each element is fed by its own sinusoidal source.

total number of elements, the amplitude of each element or the spacing between them. According to Balanis [6], the radiation pattern of a linear array can be obtained as the product of the individual element's pattern, assuming that all of them are exactly the same, and an array factor (AF), with a slight modification to the reference system for the azimuth angle (θ), as shown in Equations 2.5 and 2.6. Of course, the radiation pattern's plot is obtained by squaring the values of magnitude of the electric field, and the converting them to logarithmic scale (dB).

$$\bar{E} = \bar{f}_e(\theta) AF \tag{2.5}$$

$$AF = \sum_{n=1}^{N} a_n e^{j(n-1)kd(\sin(\theta) - \sin(\theta_0))} \tag{2.6}$$

Where:

- $\bar{E}$ is the electric field.
- $\bar{f}_e(\theta)$ is the individual radiation pattern.

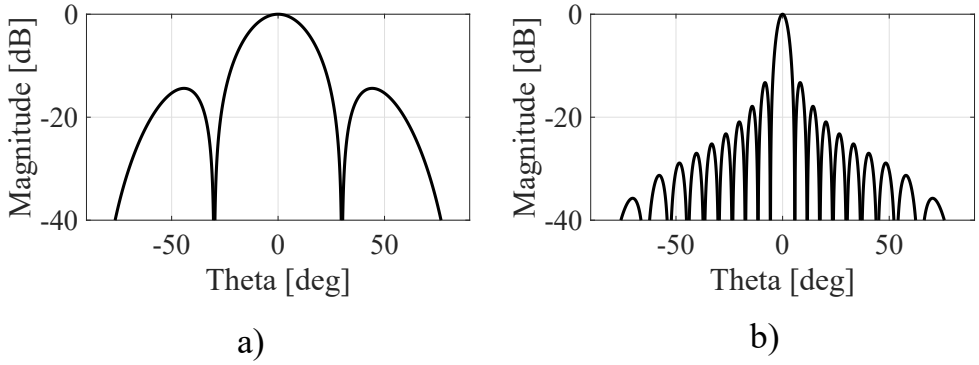

Figure 2.6: MATLAB simulations of the normalized radiation patterns of two arrays with a spacing of half wavelength and uniform amplitudes for (a) 4 elements and (b) 20 elements.

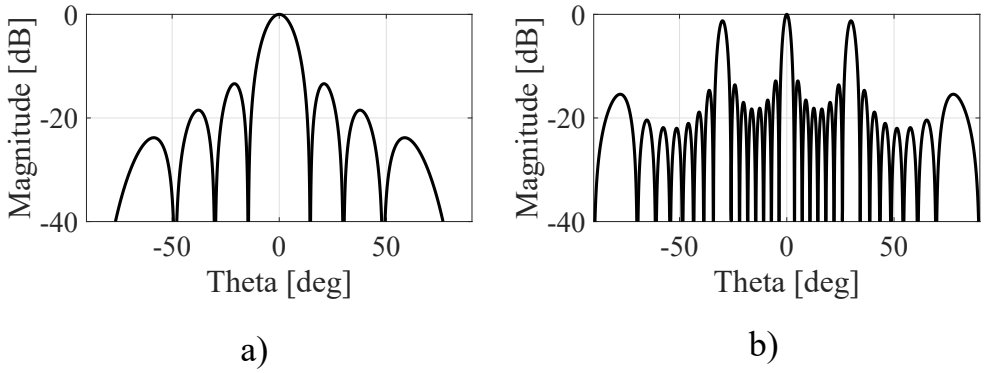

Figure 2.7: MATLAB simulations of the normalized radiation patterns of two arrays with 8 elements and uniform amplitudes for (a) spacing of half wavelength and (b) spacing of two wavelengths.

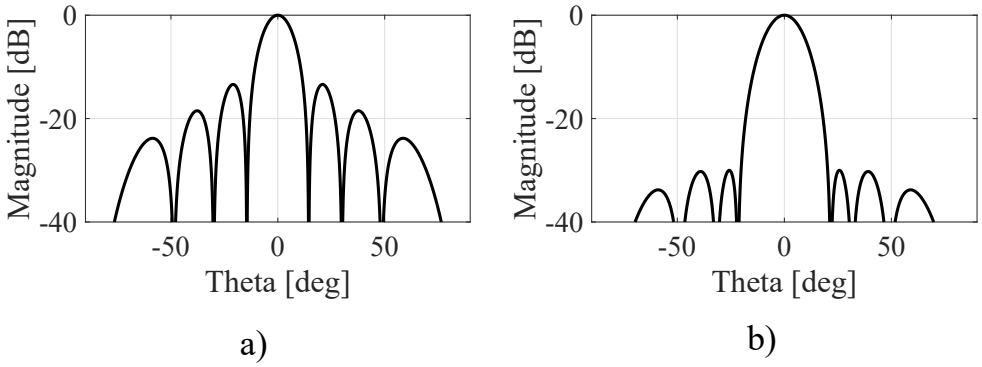

Figure 2.8: MATLAB simulations of the normalized radiation patterns of two arrays with 8 elements and a spacing of half wavelength for (a) uniform amplitudes and (b) amplitudes with Taylor tapering.

- N is the number of elements.
- a_n is the amplitude of the excitation of each element.
- k is the propagation constant.
- d is the spacing between elements.
- θ is the respective azimuth angle.
- θ_0 is the desired scanning angle.

Now, by approximating the individual element's radiation pattern component as a cosine function, in which $\bar{f}_e(\theta) = \cos\theta$, Equations 2.5 and 2.6 were implemented in MATLAB for different cases. Figure 2.6 shows the radiation patterns of two arrays with 8 and 20 elements. We can see that the beamwidth is greatly reduced for the second case, and more sidelobes also appear. This is in agreement with the idea that a larger electrical size of the antenna is required to increase the directivity and reduce the beamwidth. Figure 2.7 displays two radiation patterns of arrays with 8 elements, but with different spacing (d). The second panel shows a narrower beamwidth, but it also comes with other undesired high-power beams, called grating lobes, located at $\theta = \pm 30^\circ$. This is because the electrical size has effectively increased while having significant empty spaces in between elements. Lastly, Figure 2.8 demonstrates the result of modifying the amplitudes of the excitations of each element in the array (a_n) according to a Taylor distribution (which will be explained in more detail in chapter 3). This different distribution of amplitudes allows to reduce the power of the sidelobes, but it broadens the beamwidth.

2.6 Refraction theory

The theory of corrective lenses is based on the theory of refraction of light. This phenomenon happens when a ray of light changes from one medium to another, causing its direction to slightly change. Kingslake [40] states that the fundamental expression that

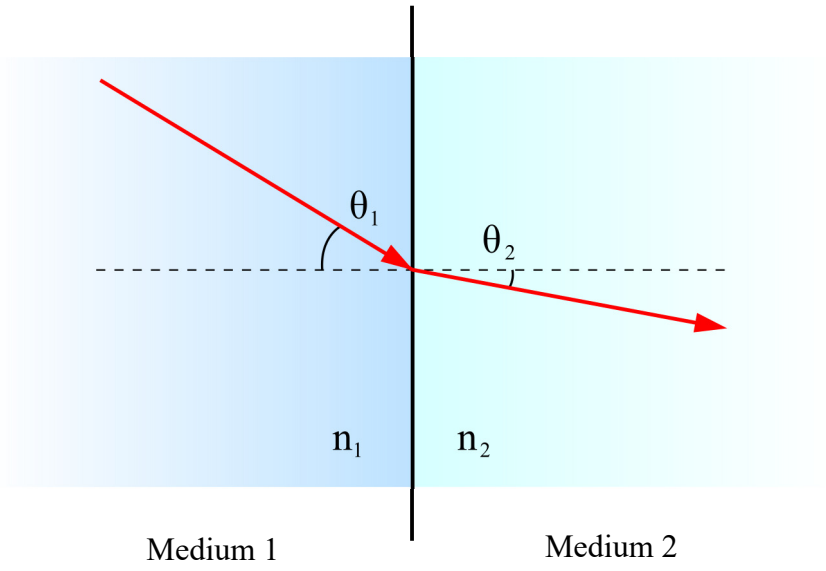

Figure 2.9: Refraction of a ray of light (red arrow), going from Medium 1 to Medium 2. Each medium has a different index of refraction.

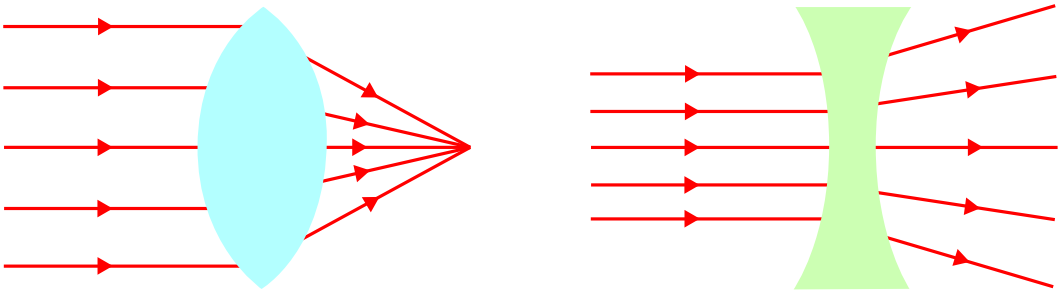

a) b)

Figure 2.10: Schematic of rays of light going through (a) convex and (b) concave lenses.

explains refraction is given by Snell's Law, which is shown in Equation 2.7. A visual representation of the parameters of this equation can be seen in Figure 2.9.

$$n_1 \sin(\theta_1) = n_2 \sin(\theta_2) \tag{2.7}$$

Where:

- n_1 and n_2 are the indices of refraction of the two media.
- θ_1 and θ_2 are the angles between the incident and refracted rays respectively, with

respect to the normal.

Basic optical lenses refract light in different ways based on their geometry. They could be either convex or concave, making the beams of light converge or diverge, respectively. Figure 2.10 shows both cases. It is important to also mention that they work both ways. For instance, the portrayed convex lens can make parallel beams of light converge into one point (from left to right), or make radially radiated beams from that point go parallel to each other (from right to left). For antennas, lenses are fabricated in order to focus the radiated energy in broadside, therefore acting as a convex lens. My present work, however, will demonstrate how to do that with a planar lens, instead of a curved one. Microwave frequency lenses, however, use the dielectric constant of the material (ε_r) instead of the index of refraction (n). These two values, however, are closely correlated as shown in Equation 2.8, and throughout the next the usage of the material's dielectric constant to achieve necessary phase changes will be investigated.

$$n = \sqrt{\varepsilon_r} \tag{2.8}$$

2.7 Summary

This chapter explained the concepts of radiation pattern, directivity, gain, beamwidth and phase center of an antenna. The radiation pattern of antennas will be one of the main focuses in the next chapters. This is because both the beamwidth reduction that is seeked with the usage of lenses, and the careful placement of nulls and grating lobes in virtual arrays are obtained by inspecting the expected radiation patterns. The phase center is also relevant to this work, as the focal distance of a dielectric lens must be calculated with respect to that point. Additionally, an introduction to antenna arrays was given, along with the main equation of the radiated fields. Furthermore, some examples of radiation patterns for linear arrays when modifying multiple parameters such as the number of elements, the

spacing and the amplitude tapering were shown. All of these parameters are necessary for carefully tweaking the desired radiation patterns, in order to achieve a successful virtual array. Lastly, refraction theory and basic lenses were also discussed, and those concepts are the foundation for designing a flat dielectric lens that will radially change its dielectric constant instead of having a concave or convex curvature.

Chapter 3

Design Procedure and Tradeoffs

The mathematical procedures to design both dielectric lenses and virtual arrays are presented in this chapter. The dimensions of the lens were obtained by approximating it as a radiating aperture antenna, whereas the required dielectric constant profile was calculated by obtaining the phase profile at each point of the lens, and then compensating them. As for the virtual arrays, they are synthesized by placing the nulls of one pattern in the same angular direction of the grating lobes of the other one, with some additional considerations that will be explained later. Lastly, a tradeoff analysis is also performed for the number of elements versus the effective two-way beamwidth reduction, where the used number of elements is compared with the respective beamwidth reduction.

3.1 Dielectric Lenses

3.1.1 Dimensions

A dielectric lens can be considered as a radiating source similar to a circular aperture antenna. Just like that type of antenna, the resulting beamwidth changes according to the size of the aperture. An expression to obtain the half-power beamwidth of this type of aperture is shown by Balanis [6] and is expressed in Equation 3.1, but solving for the

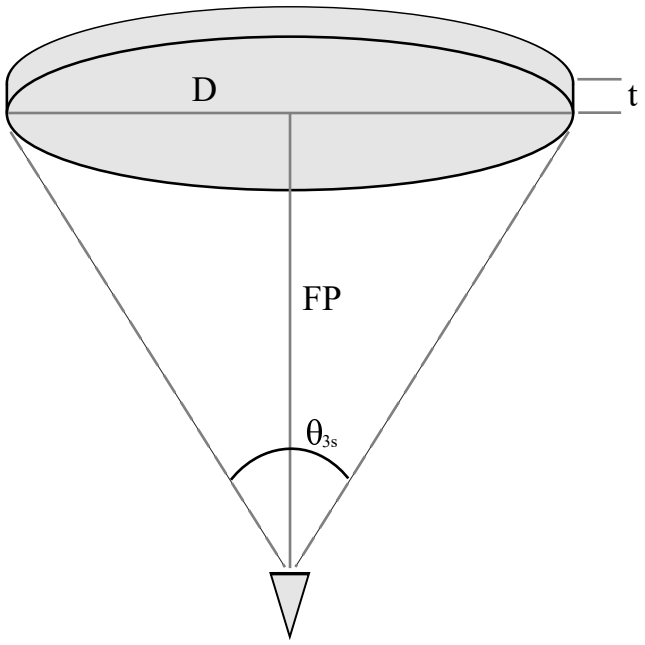

Figure 3.1: Geometry showing the relationship between the desired illumination of the lens (given by the angle θ_{3s}, which stands for the 3 dB beamwidth of the source) and the focal point (FP). D is the diameter of the lens, and t is its thickness.

necessary radius to obtain a certain desired beamwidth.

$$R = \frac{29.2\lambda_0}{\theta_{3o}} \tag{3.1}$$

Here, R is the lens radius, λ_0 is the free-space wavelength of the frequency of our source, and θ_{3o} is the desired half-power beamwidth as the output of the lens.

3.1.2 Focal Point and Sidelobes

The focal point of this type of flat lens can be obtained by considering how much of the source radiation we want to be captured and affected by the lens. Figure 3.1 shows the setup and the applied geometry to calculate the focal point. Equation 3.2 allows for a quick calculation of this distance, considering the value of θ_{3s} as the angle containing all the desired source radiation captured by the lens. It is important to mention that this focal

point is relative to the phase center of the antenna.

$$FP = \frac{D}{2\tan\left(\frac{\theta_{3s}}{2}\right)} \tag{3.2}$$

3.1.3 Dielectric Constant Profile

A dielectric constant profile is required in order to achieve a phase shift across the lens that reorients the source radiation as a plane wave. This profile must try to compensate the differences in phase and create a planar wave front. Additionally, in order to obtain a feasible design, the profile is discretized into multiple concentric rings of equal permittivity, as shown in Figure 3.2. This has been similarly performed before [18], but the equations to use in my present work have been independently derived from scratch.

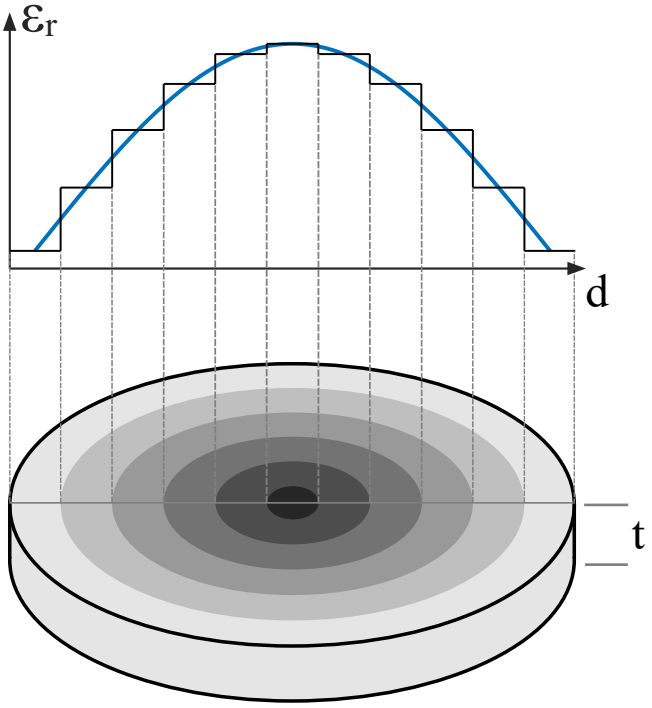

Figure 3.2: Discretized dielectric constant profile across the concentric rings of a flat lens. The blue line in the plot represents the desired profile, and the black line represents the different steps taken in the lens. The vertical axis is the dielectric constant (ε_r),the horizontal axis is the radial distance in the lens (d), and t is the lens thickness.

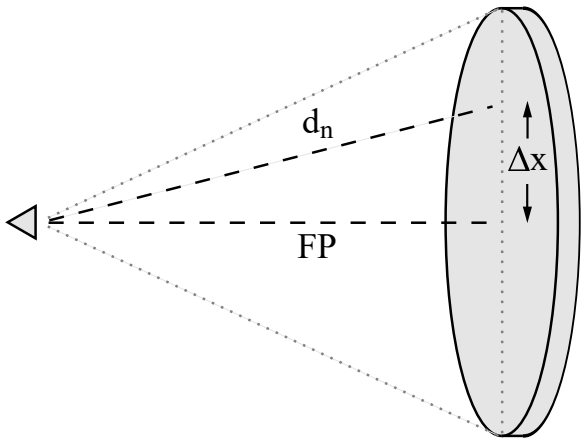

Figure 3.3: Geometry showing the variables used to calculate the lens profile. FP is the focal point, d_n is the distance between the source and the nth concentric ring, and Δx is the distance between said ring and the center of the lens.

In order to calculate the phase at each point of the lens, the distance from the source to each one of those points must be calculated.

$$d_n = \sqrt{(\Delta x)^2 + (FP)^2} \tag{3.3}$$

The variables in Equation 3.3 can be better visualized in Figure 3.3. Additionally, the subscript "n" represents one of the different concentric rings (each ring will have a particular distance from the source). Now, the respective phases at each point are calculated using Equation 3.4.

$$\phi_n = \frac{2\pi d_n}{\lambda} \tag{3.4}$$

Where:

- ϕ_n is the phase at the nth ring.
- d_n is the distance from the source from Equation 3.3.
- λ is the wavelength.

Once the phases have been calculated, a minimum dielectric constant value (ε_1) has to be chosen as a design criteria. This value will be placed in the outer ring of the lens since that is the one with the lowest permittivity, as shown in Figure 3.2. With this value, the phase shift obtained in the last ring is calculated.

$$\Delta\phi_1 = \frac{2\pi\sqrt{\varepsilon_1}tf}{c} \tag{3.5}$$

Where:

- $\Delta\phi_1$ is the phase shift of the last ring.
- ε_1 is the dielectric constant of the last ring.
- t is the lens thickness.
- f is the frequency.
- c is the speed of light.

Lastly, we obtain the equation that will give us the dielectric constant profile.

$$\varepsilon_n = \left[\frac{(\Delta\phi_1 + \phi_{n_{diff}})c}{2\pi tf}\right]^2 \tag{3.6}$$

Here, we have the same variables as Equation 3.5, with the addition of ε_n, which is the desired dielectric constant, and $\phi_{n_{diff}}$, which is the difference between the maximum value of phase $\max(\phi_n)$ and the respective value of the phase in the point that we want to analyze in the lens (ϕ_n).

$$\phi_{n_{diff}} = \max(\phi_n) - \phi_n \tag{3.7}$$

It is important to understand that while Equation 3.6 can provide a profile for any value of thickness, sometimes this quantity has to be adjusted in order to obtain a realizable profile. This is because a lower thickness means a higher required dielectric constant, and this is a physical limitation of the material to be used.

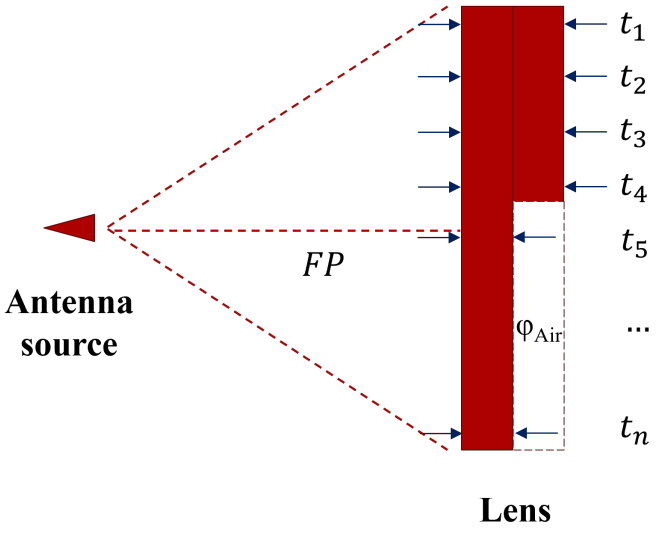

Figure 3.4: Schematic of an example of a conformal lens with different values of thickness. The focal point (FP), variable thickness (t_n) and phase shift of air (ϕ_{Air}) are indicated.

Additionally, this equation can be slightly adjusted to also work for a lens that is not just purely planar as the ones studied in the literature, so it could also help design conformal lenses. Following Figure 3.4, we would have to account for the phase shifts of air in the sections that do not have the maximum value of thickness. Moreover, the value of t would now be t_n in order to correctly indicate that it refers to the value of the thickness at the particular point in which we want to calculate the dielectric constant. The obtained expression for this case is Equation 3.8.

$$\varepsilon_n = \left[\frac{(\Delta\phi_1 + \phi_{n_{diff}} - \phi_{\mathbf{Air}})c}{2\pi \mathbf{t_n} f}\right]^2 \tag{3.8}$$

The value of ϕ_{Air} can be calculated in a similar way as Equation 3.4, just replacing the distances d_n for the remaining thickness values at each point of the lens.

3.1.4 Quantization errors

Now that the dielectric constant profile has been calculated and discretized into multiple concentric rings, the effect of quantization errors must be analyzed. As it was shown in Figure 3.2, we have a continuous profile that we would ideally have, and then multiple levels that we are discretizing it into, for a more realistic approach when it comes to fabricating the lens. Considering that each value of dielectric constant corresponds to a particular phase shift that must be achieved in the lens, an expression for the mean square error of the phase quantization errors was obtained from Mailloux [28], and it is portrayed in Equation 3.9

$$\bar{\Phi^2} = \frac{1}{3}\frac{\pi^2}{2^{2N}} \tag{3.9}$$

Where:

- $\bar{\Phi^2}$ is the mean square error of the phase quantization errors.
- N is the number of bits.

Since there are no bits in our case, but only a certain number of discretized levels, we can change the number of bits N for the number of levels n, where $n = 2^N$, obtaining Equation 3.10.

$$\bar{\Phi^2} = \frac{1}{3}\frac{\pi^2}{n^2} \tag{3.10}$$

Lastly, since these equations give us the errors in radians, they can only be applied for cases in which the phase quantization errors involve discrete levels between 0 and 2π. Taking into account that the necessary phase shifts that are achieved with dielectric lenses are not necessarily in that range, an expression in which the phase error is represented in percentage was derived, and it is shown in Equation 3.11.

$$\bar{\Phi^2}\% = \frac{1}{3}\frac{\pi^2}{n^2}\frac{100}{2\pi} = \frac{50}{3}\frac{\pi}{n^2} \tag{3.11}$$

Using this equation, we can calculate the phase quantization errors for a different number of levels, or concentric rings. Some of these values are displayed in Table 3.1.

Number of levels (n)	4	5	6	7	8	9
Phase errors [%]	3.2725	2.0944	1.4544	1.0686	0.8181	0.6464

Table 3.1: Phase quantization errors for different number of levels in the discretized dielectric constant profile.

The resulting phase errors are very small regardless of the number of concentric rings, but it is also important to understand that small errors in phase could still affect our desired planar wave at the output of the lens. Therefore, a number of rings of around 6 or more is encouraged, due to the errors being close to or less than 1%.

3.1.5 Unit Cells

In order to build a symmetrical and periodical structure, hexagonal unit cells were used. This is because they can be easily assembled together, as shown in Figure 3.5. The dielectric constant of each unit cell was modified by adding a hole to it, which can be considered as an air cylinder. Following the Van Beek model [41], Equation 3.12 can be used to calculate the effective dielectric constant of these anisotropic unit cells.

$$\varepsilon_{eff} = \varepsilon_b + \frac{f}{3}\frac{(\varepsilon_a - \varepsilon_b)(5\varepsilon_b + \varepsilon_a)}{(\varepsilon_b + \varepsilon_a)} \tag{3.12}$$

Here, ε_{eff} is the effective dielectric constant, ε_a is the permittivity of air, ε_b is the permittivity of the lens' material, and f is the fractional volume. For a hexagonal unit cell, the value of f can be easily calculated by dividing the volume of a cylinder by the volume of a

hexagonal prism. Equation 3.13 shows the reduced expression for obtaining this value.

$$f = \frac{2\pi R^2}{3\sqrt{3}s^2} \tag{3.13}$$

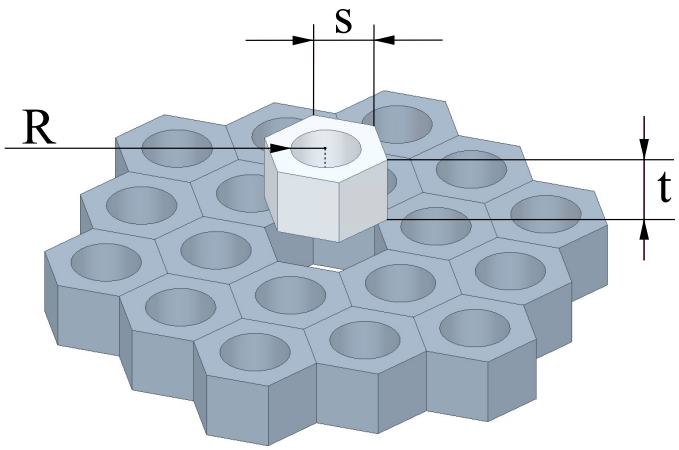

Figure 3.5: Assembly of Hexagonal Unit Cells into a large, periodical structure. R is the radius of the hole, s is the side of the hexagon and t is the thickness of the unit cell.

Additionally, Jehangir et al. [41] analyzed the required size of the unit cell for the mixing theory and the simulations to be in agreement. A size of $0.5\lambda_g$ or less is necessary for this concept to work, and a size of $0.1\lambda_g$ is recommended (where $\lambda_g = \lambda_0/\sqrt{\varepsilon_r}$). Additionally, if we want our lens to work at a wide frequency band, the unit cells have to be even smaller, so that their size does not exceed $0.5\lambda_g$ at the higher frequencies. This is because the frequency is inversely proportional to the wavelength, and even though the absolute size of the unit cell is the same, it will represent more wavelengths in higher frequencies.

Lastly, Figure 3.6 shows how the hexagonal unit cells matrix can be used to form a larger structure that approximates concentrical rings of different effective dielectric constants, represented by the different shades of grey.

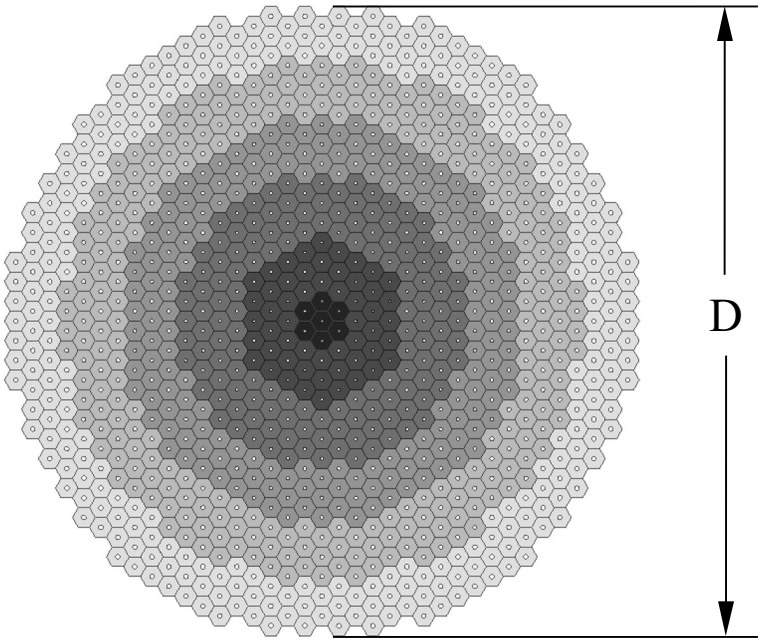

Figure 3.6: Top view of an assembled lens. The different shades of gray represent different values of dielectric constant. D is the diameter of the lens.

3.1.6 Tradeoffs

Equation 3.6 shows that the required dielectric constants in the profile are inversely proportional to the square of the thickness. Therefore, thicker lenses are required if a low dielectric constant material is used. For instance, Figure 3.7 shows the dielectric constant profiles for two lenses with the same specs, but with different values of thickness. The thinner lens requires a different profile with a higher maximum dielectric constant than the thicker lens. Therefore, a material with a higher permittivity is needed if the thin lens is to be fabricated. Additionally, the value of $\phi_{n_{diff}}$ in Equation 3.6 is inversely proportional to the focal point. This is because the greater the distance is between the source and the lens, the lower the influence of Δx in Equation 3.3. Following Equations 3.4, 3.5 and 3.6, we can see the relationship between focal distance and required dielectric constant being inversely proportional. Figure 3.8 shows that a greater illumination of the lens via a lower

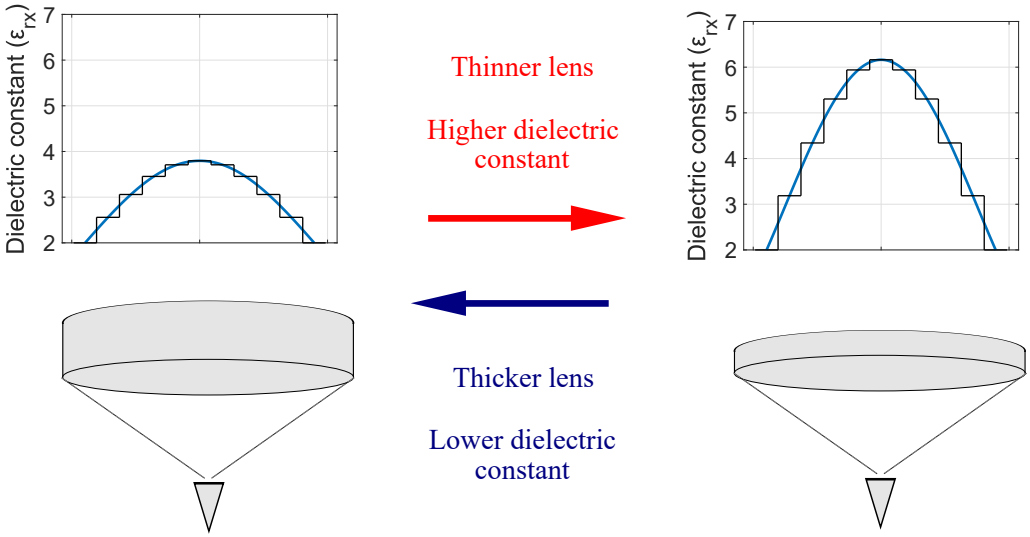

Figure 3.7: Comparison between the required dielectric constant profiles of two lenses with different values of thickness.

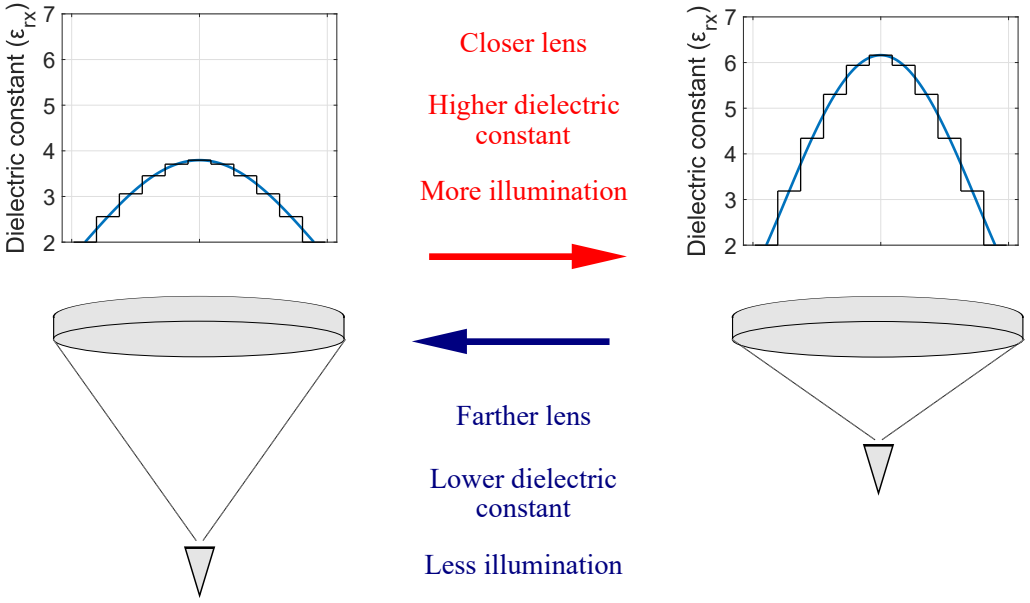

Figure 3.8: Comparison between the required dielectric constant profiles of two lenses with different values of focal point.

focal distance can only be achieved if we use a material with a higher dielectric constant.

Additionally, one last tradeoff can be described by comparing this type of Gradient Index (GRIN) planar lenses with respect to common concave or convex lenses. Taking into

account that the material that is used for the lens has not just a real value of permittivity, but also an imaginary one, there will be losses in the dielectric. A curved lens would be less efficient as it would have different values of changing thickness, which would lead to having different losses. On the other hand, a flat lens with the same material would have a more homogeneous loss across all its surface. Of course, it would not be perfect due to the presence of holes of different sizes, but it would be more consistent than a non-flat one.

3.2 Virtual Arrays

3.2.1 Number of Virtual Elements

Common applications of antenna arrays use a half-wavelength spacing between elements. This is because greater separation values would contribute with the appearance of a phenomenon called grating lobes, in which the energy is distributed in a different way, presenting big undesired energy leakages in multiple directions and making the system inefficient. This effect, however, can be taken care off if we consider that communications and radar systems consist of transmission and reception arrays, whose whole two-way radiation pattern will result in the superposition of both individual patterns (see Figure 3.10). This way, even though grating lobes may appear by changing the element spacing, they can be methodically cancelled with nulls from the other pattern, a concept called virtual arrays.

As we apply the virtual array concept, patterns with a narrower mainbeam can be obtained. A good analogy is to look at the generated two-way pattern as a resulting single array with a different number of elements. This new virtual array can be computed by applying a convolution to the ampltiude weight vectors of the excitations of the transmission and reception arrays. For instance, if we design the following vectors as the excitations of two 3-element arrays:

$$A_{Tx} = [1, 1, 1], \quad A_{Rx} = [1, 1, 1]$$

Where A_{Tx} and A_{Rx} are the amplitude weight vectors for the transmission and reception array, respectively. Additionally, each "1" represents the amplitude excitation weight of each antenna, and the distance between elements is half wavelength. The equivalent virtual antenna array that would generate the same pattern as the two-way pattern of this system is given by the convolution of both vectors, and is represented as A_{eq}.

$$A_{eq} = A_{Tx} * A_{Rx} = [1, 2, 3, 2, 1]$$

This means that our 6-element two-way system is equivalent to a 5-element virtual array, whose amplitude weights have a gradient.

In order to achieve the narrowest possible beamwidth, the maximum number of elements (in this case, virtual elements) has to be obtained [6]. This can be done by exactly positioning the nulls of one array in the grating lobes of the other one. This can be done after choosing which array will have the grating lobes. As will be further shown, the array that can support amplitude tapering in virtual arrays is the one that has the grating lobes, and since tapering the transmission array is not optimal due to a desired maximum power transmission, the grating lobes have to be in the reception array.

First, we need to identify the position of the nulls of a uniform array (our transmission array). Equation 3.14 was obtained and slightly modified from Balanis [6] to appropriately work with our coordinate system, allowing us to obtain the angular positions of all the nulls in the radiation pattern.

$$\theta_n = \sin^{-1}\left(\pm\frac{n\lambda}{Nd}\right) \tag{3.14}$$

Where:

- θ_n is the angular position of the nulls, in degrees.
- n is a constant that can take values of positive integers.

- λ is the wavelength.
- N is the number of elements in the array.
- d is the spacing between elements.

As for the position of the grating lobes on our reception array, we can easily derive it from Equation 3.15, obtained from Skolnik [42].

$$|\sin(\theta_g) - \sin(\theta_0)| = \frac{n\lambda}{d} \tag{3.15}$$

Where:

- θ_g is the angular position of the grating lobes, in degrees.
- θ_0 is the angle at which the array is steered to scan.
- n is a constant that can take values of positive integers.
- λ is the wavelength.
- d is the spacing between elements.

If we consider the array in broadside, that is, with the beam pointing at 0° ($\theta_0 = 0$), we have Equation 3.16.

$$\theta_g = \sin^{-1}\left(\pm\frac{n\lambda}{d}\right) \tag{3.16}$$

Lastly, we need to make the angles of Equations 3.14 and 3.16 equal. Given that the only difference between them is the denominator inside of the arcsine, the equation to obtain the maximum number of virtual elements reduces to Equation 3.17.

$$d_{Rx} = N_{Tx} d_{Tx} \tag{3.17}$$

Where:

- d_{Rx} is the element spacing for the receiving array.

- N_{Tx} is the number of elements in the transmitting array.
- d_{Tx} is the element spacing for the transmitting array.

Following the same example that was being used before, if we want to obtain the maximum number of virtual elements, we need the following equation to hold true: $d_{Rx} = 3(0.5\lambda) = 1.5\lambda$, therefore:

$$A_{Tx} = [1, 1, 1]$$

$$A_{Rx} = [1, 0, 0, 1, 0, 0, 1]$$

The resulting convolution will be a 9-element array full of ones:

$$A_{eq} = A_{Tx} * A_{Rx} = [1, 1, 1, 1, 1, 1, 1, 1, 1]$$

The maximum number of virtual elements was achieved, which will always be the same as the product of the number of Tx elements and the number of Rx elements. This same example is explained in a graphic way in Figure 3.9, showing the synthesis of a virtual array by applying a convolution. Equation 3.17 can be better understood from Figure 3.9b, given that the spacing between elements in reception has to leave room for the whole transmission array to overlap with each element before starting to overlap with the next one. Another option that achieves this is the modification of the spacing between the transmission elements instead. However, as is further shown, amplitude tapering in virtual arrays has to be applied in the array that has the grating lobes, and tapering the Tx array is not optimal since power transmission is always desired to be kept at maximum. Figure 3.10 shows the comparison between the two-way normalized patterns of the aforementioned example when we have the common half-wavelength spacing for both arrays, and when we modify the spacing for the Rx array.

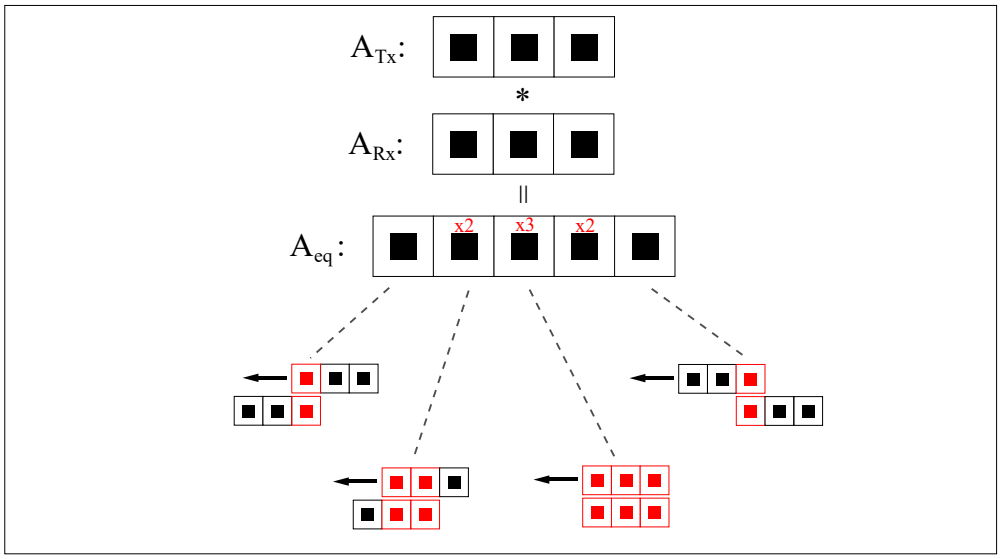

a)

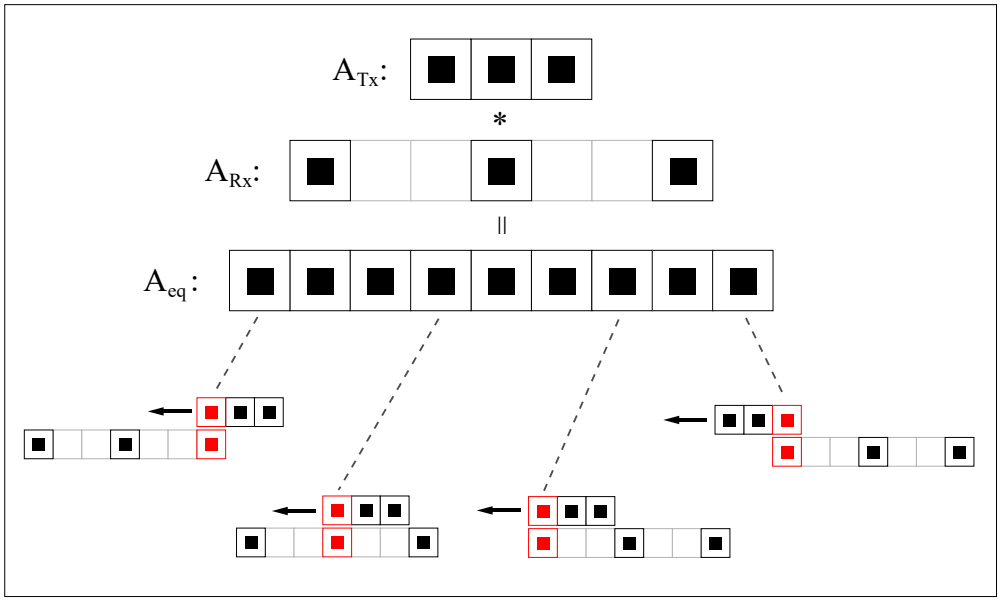

b)

Figure 3.9: Visual demonstration of the synthesis of a virtual array applying the concept of convolution for (a) half-wavelength spacing between elements in both arrays and (b) modifying the spacing in reception to 1.5 wavelengths. In both cases, one array moves with respect to the other, and the virtual array is the resulting overlap between them.

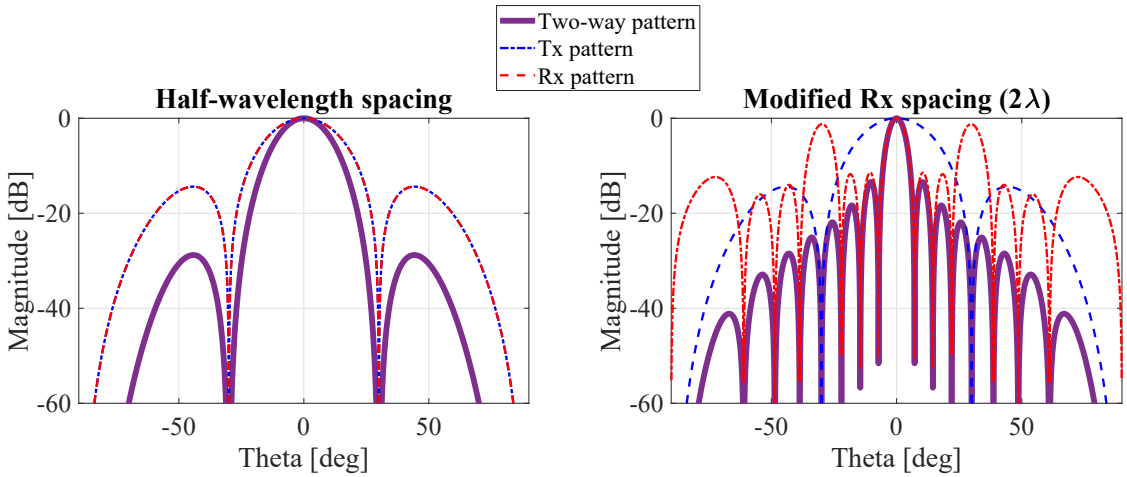

Figure 3.10: Comparison of the normalized two-way patterns of two 4-element arrays (Tx and Rx) with a spacing of half-wavelength (0.5λ) and two-wavelength (2λ) in reception.

3.2.2 Grating Lobes and Scanning

Grating lobes are obtained when the spacing between elements exceeds one wavelength [6], following the array factor equation in case all the elements are considered the same. They also appear when applying beam steering to an array with a spacing greater than half-wavelength. By exactly cancelling out the grating lobes of the Rx pattern with the nulls of the Tx pattern by applying Equation 3.17, it is guaranteed that the two-way pattern will not have any grating lobes. This is also possible because the spacing between the Tx elements is kept as half-wavelength, with its grating lobes only appearing after scanning around 90°. Therefore, scanning can be achieved by obtaining a periodical cancellation of the grating lobes as they appear while we steer out of broadside. Two different steering angles are shown in Figure 3.11 for the same case with 4-elements in Tx and 4-elements in Rx. The gain reduction of the mainbeam in the 50° plot is caused by the individual radiation pattern roll-off, in this case a cosine function. This affects the two-way pattern twice as both the transmission and reflection arrays are influenced by it. Antennas with a broader individual radiation pattern would be required to increase the beam steering capabilities over $50°$.

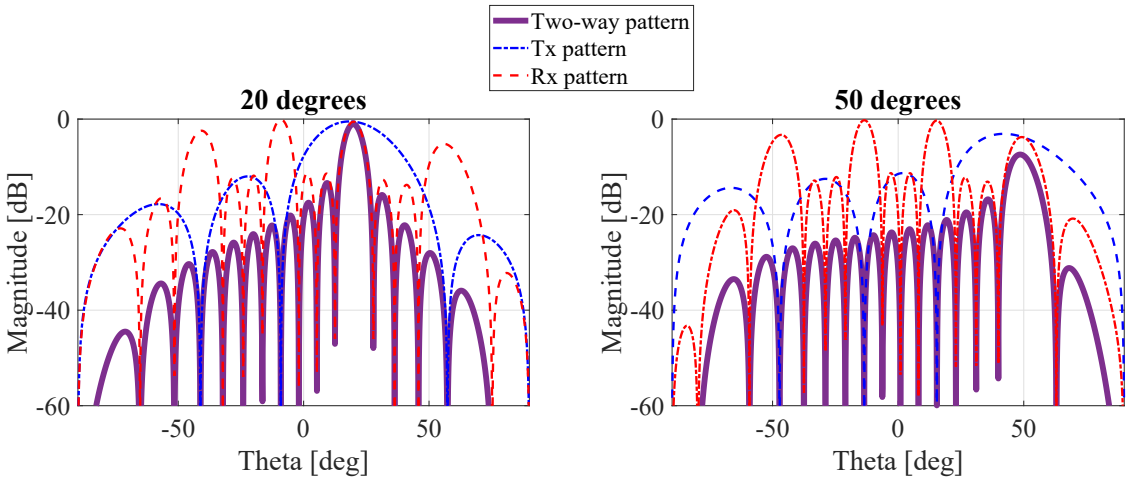

Figure 3.11: Beam steering capabilities of two 4-element arrays (Tx and Rx), applying the virtual array concept.

3.2.3 Taylor Tapering

After obtaining the narrowest achievable beamwidth due to the maximum possible number of virtual elements, another metric that can be optimized is the sidelobe level. This is because the obtained two-way pattern has a uniform distribution, i.e., an array full of ones as a result of the convolution, with peak sidelobes of about -13.46 dB [6]. One way to reduce them is by applying an amplitude taper, in this case, Taylor distributions [43] will be analyzed. It is important to notice that in a common radiation pattern, the position of the nulls will slightly change if we apply amplitude tapering. This is not ideal if we want to apply the Virtual Array concept by cancelling out the peaks and nulls. However, Taylor tapering only affects a certain number of sidelobes and their respective null positions. As a consequence, when we apply a Taylor distribution to an array with a greater spacing than half wavelength, which if we follow our prior guidelines, this happens to the Rx array, the periodical pattern of grating lobes will stay unchanged. This means that the angular position of each grating lobe will stay the same no matter how much we reduce the sidelobe level (SLL) by, as is shown in Figure 3.12. The only slight change in the grating lobes is

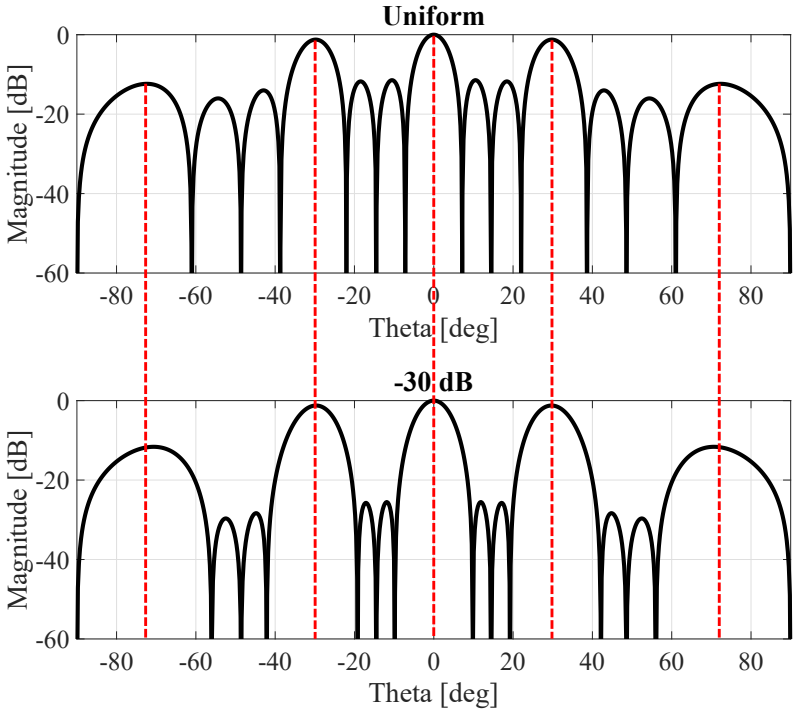

Figure 3.12: Grating lobe periodicity for a 4-element array with two-wavelength (2λ) spacing for uniform distribution and -30 dB Taylor. While the nulls are not in the same angular positions, the grating lobes are.

that they will become a little broader as we reduce the SLL in the Taylor distribution, just like in any array. Figure 3.13 shows the implementation of Taylor tapering on a 4-element reception array, whose spacing was determined using the aforementioned guidelines. The tapering was obtained by using the *taylorwin* command in MATLAB. The two-way radiation patterns of the system show a reduction in the sidelobe level, while maintaining the cancellation of the grating lobes. If the spacing in the transmission array is kept as half-wavelength, then no grating lobes will appear as we steer within the normal range of operation of a common phased array antenna. Therefore, beam steering can be successfully achieved given that the periodical cancellation of the grating lobes in the pattern of the reception array will keep ocurring even when we steer out of broadside. Figure 3.14 shows two different steering angles for the two 4-element arrays used in all previous cases, with

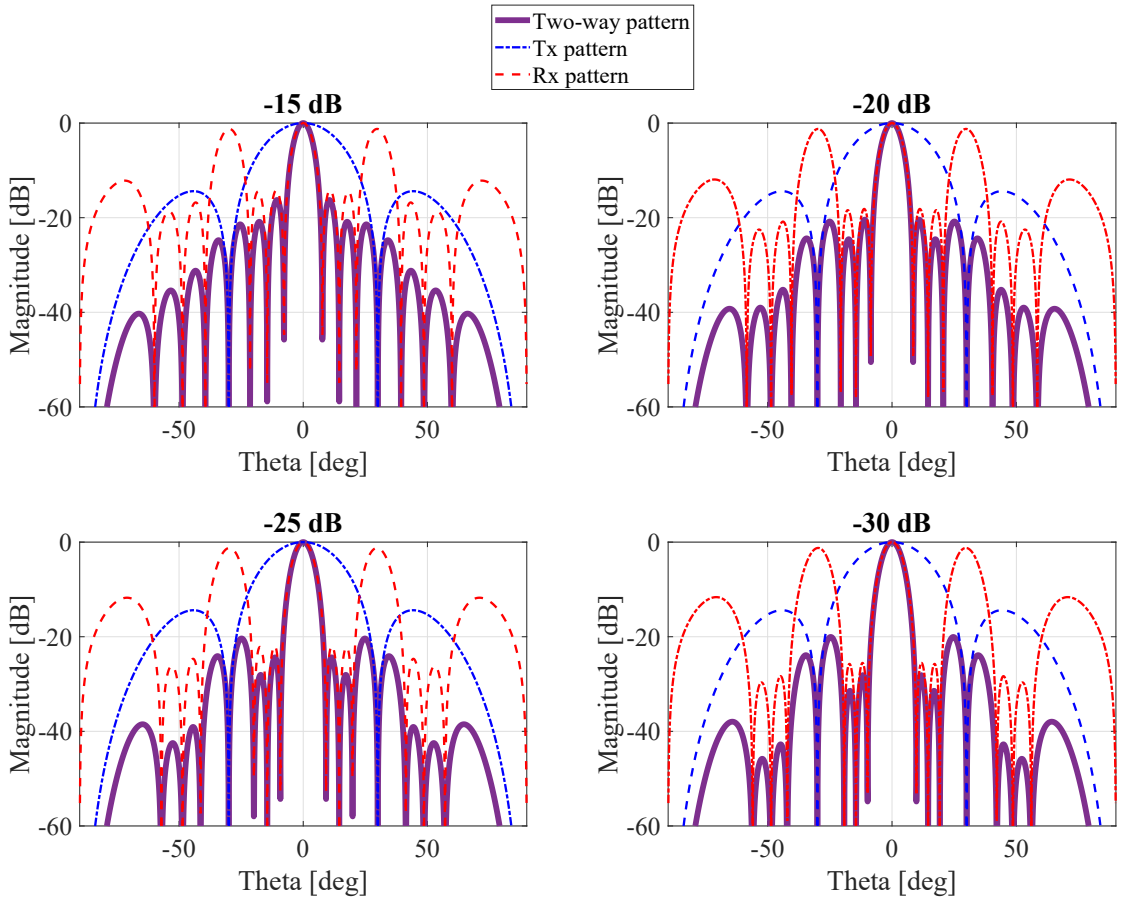

Figure 3.13: Taylor distributions (-15 dB, -20 dB, -25 dB and -30 dB) applied to the amplitudes of the reception array, maintaining the virtual array concept (4-element arrays in Tx and Rx).

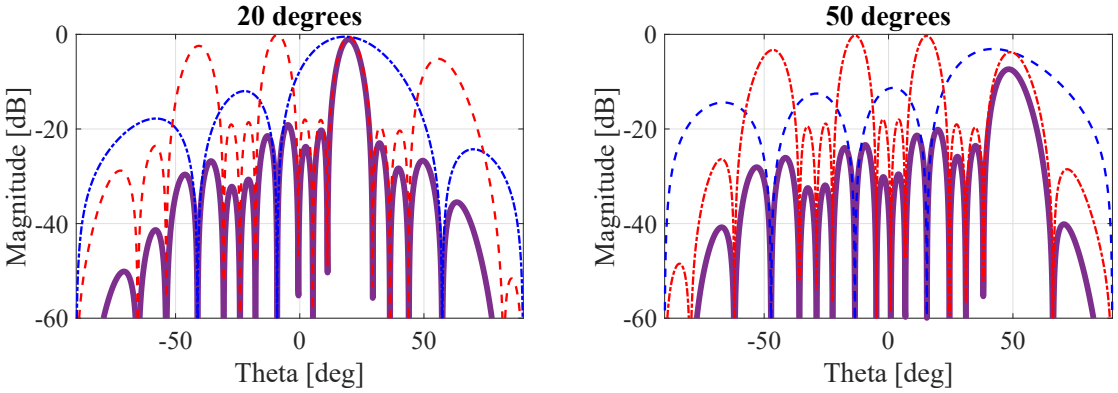

Figure 3.14: Beam steering capabilities of two 4-element arrays (Tx and Rx), with a -20 dB Taylor tapering in reception, maintaining the virtual array concept.

a 20 dB Taylor tapering in the reception array. No grating lobes are present in the two-way pattern.

3.2.4 Tradeoff analysis

First of all, the gain of the reception array will not be changed in any way by just applying a different separation of its elements. This can be validated by finding out the maximum gain in any desired steering direction, applying Equation 2.6 while considering $\theta = \theta_0$:

$$AF = \sum_{n=1}^{N} e^{j(n-1)kd(\sin(\theta_0)-\sin(\theta_0))} = \sum_{n=1}^{N} 1 \tag{3.18}$$

This means that the gain in any steered angle does not depend on the element separation in the array, but only on the number of elements itself. As a consequence, the main two features of the radiation pattern that this technique modifies are the beamwidth and the sidelobe level.

The change in the beamwidth is the main feature of this technique. Figure 3.15 shows the two-way beamwidths of two arrays when changing their number of elements for common half-wavelength spacing and for the proposed technique (obtained by Equation 3.17). The beamwidth difference is shown in Figure 3.16. The percentage reduction grows up to $\sim 90\%$ as we increase the number of elements, but the actual number of degrees that the technique reduces is greater when we have less elements (with a peak in 3 elements, showing a reduction of 13°). It is important to mention that both plots show up to 10-elements in both arrays due to the required element spacing that would take place if that number is increased (more than 5 wavelengths).

Now, regarding the sidelobes, it is mentioned by Balanis [6] that the position of the first minor lobe maxima (for obtaining the sidelobe level) for a broadside uniform linear array

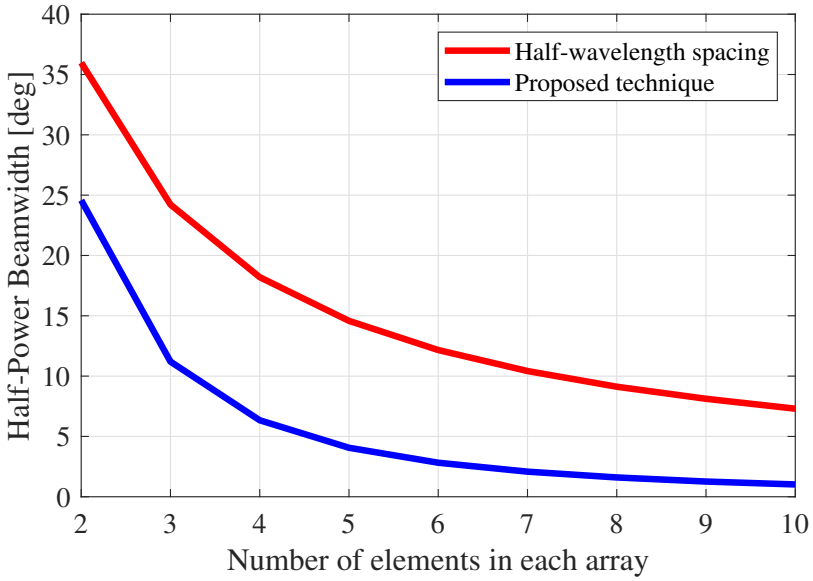

Figure 3.15: Comparison of the two-way pattern's broadside beamwidth of two arrays when changing their number of elements, for common half-wavelength spacing and for this technique.

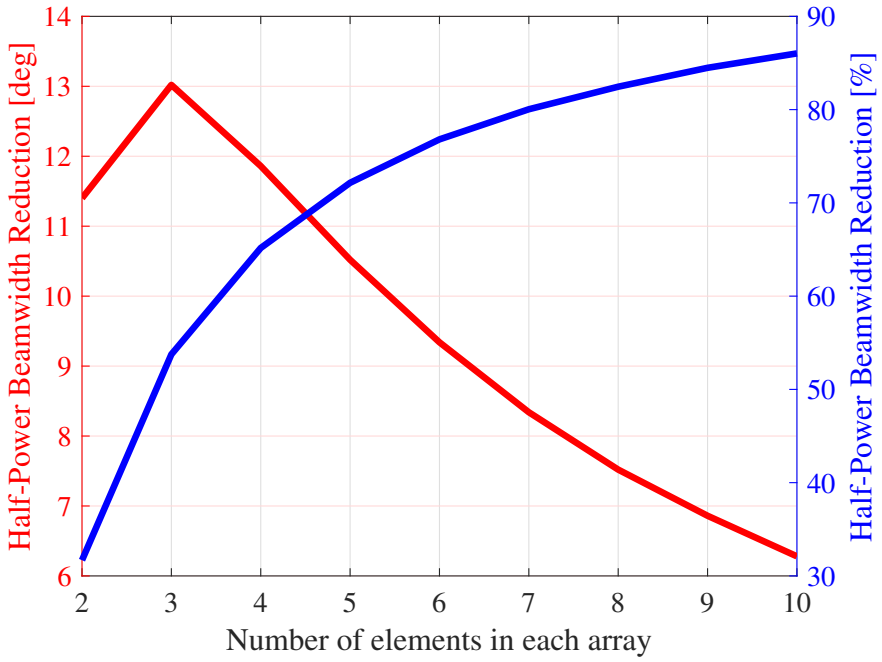

Figure 3.16: Difference of the two-way pattern's broadside beamwidth of two arrays when changing their number of elements, in degrees (left axis) and percentage (right axis)

can be calculated with:

$$\theta_s \simeq \sin^{-1}\left[\pm\frac{\lambda}{2d}\left(\frac{3}{N}\right)\right] \tag{3.19}$$

Additionally, if the array has a uniform distribution, its array factor shows a sidelobe level of approximately -13.46 dB. In a two-way system, by maintaining the spacing of the elements in both arrays as half-wavelength, the resulting sidelobe level would be -26.92 dB, which is twice the usual due to the exact overlap of the sidelobes. On the other hand, by changing the spacing following Equation 3.17 it would stay the same, due to the corresponding virtual array being a large array with a uniform distribution and equal spacing. Something to consider is that the individual element pattern can also slightly influence this sidelobe level (SLL) as shown below.

$$SLL = 10\log_{10}\left[10^{-13.46/10}\bar{f}_e(\theta_s)\right] \tag{3.20}$$

In our case, the approximation of the individual element pattern $\bar{f}_e = \cos(\theta)$ means that as the number of element increases, the influence of the individual pattern is reduced due to the proximity of the sidelobes to the main beam. This is always the case for the proposed virtual array synthesis technique, due to the maximization of the number of virtual elements. This means that the sidelobe level is almost doubled in all of the investigated cases in this work.

3.3 Summary

This chapter showed the mathematical derivations used to create a general procedure to design dielectric lenses and virtual arrays. A dielectric lens is approximated as a radiating circular aperture to match a desired beamwidth, and a dielectric constant profile is obtained by aiming to compensate for the different phase shifts at each point of the lens.

An additional equation for conformal lenses was derived and explained, allowing for more flexibility than the equations shown in the literature. Quantization errors are also explained as the calculated profile was discretized into multiple levels. Hexagonal unit cells with air cylindrical holes are designed to achieve this dielectric constant profile, and then assembled in a large structure, resembling concentrical rings. Tradeoffs are also given and discussed, explaining that the required dielectric constant of the material is inversely proportional to both the thickness of the lens and its focal distance. Regarding virtual arrays, the linear array fields equation was used alongisde the formulations for nulls and grating lobes to obtain a simple equation that allows to constantly obtain the maximum achievable number of virtual elements, effectively reducing the two-way pattern beamwidth of an antenna system. Beam steering and amplitude tapering were also discussed and examples were given. It was demonstrated that the proposed method allows the use of both of them, even when applied simultaneously, achieving scanning up to 50° and amplitude tapering that can reduce some sidelobes down to -30 dB. These theoretical results support the effectiveness of this new methodical procedure to design virtual arrays that are not limited in scanning and tapering capabilities. Additionally, tradeoffs between beamwidth reduction and sidelobe level were discussed.

Chapter 4

Results

The design, simulation, implementation and measurement of both the dielectric lens and the virtual array based on the methodology from previous sections are presented on this chapter. The characterization of the lens' material was performed, which allowed to establish the base upon which the lens had to be built. The design was tested in Ansys HFSS and then fabricated using a resin 3D printed. The lens was placed in a frame with its respective source and measured in a far field chamber. Regarding the Virtual Arrays, two 4x1 arrays with different spacing were simulated in Ansys HFSS using the domain decomposition technique. The concept was then verified by fabricating two series-feed antenna arrays with the same values of spacing, whose measured patterns were then overlapped and compared.

4.1 S-band dielectric lens design and simulation

To begin with, it was decided that the fabrication of the lens would be performed using additive manufacturing. The used device was a Form3 stereolithography (SLA) 3D resin printer from the company Formlabs, with their resin called "Grey V4", which was available in the facilities of the Advanced Radar Research Center. A picture of this printer, alongside two other machines for cleaning and curing the pieces are displayed in Figure 4.1. The

Figure 4.1: FormLabs additive manufacturing equipment. Form3 3D printer (left), Isopropil alcohol cleaner (center) and UV light curing device (right).

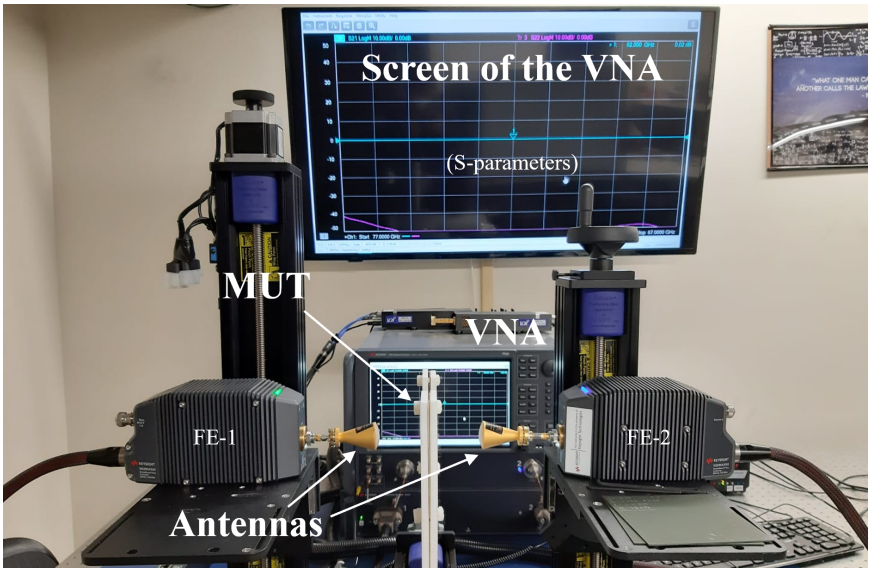

Figure 4.2: Material characterization setup and its components at the mmWave and subterahertz lab. in the Radar Innovations Laboratory.

features of the aforementioned resin were first measured using a free-space material characterization setup that is shown in Figure 4.2. It comes with a Vector Network Analyzer (VNA), two frequency extenders for 77-87 GHz, two spot-focused lens horn antennas and a holder for the Material Under Test (MUT). A small sample of Grey V4 resin with dimensions of 14 mm x 14 mm x 1 mm was printed for characterization, which is visualized

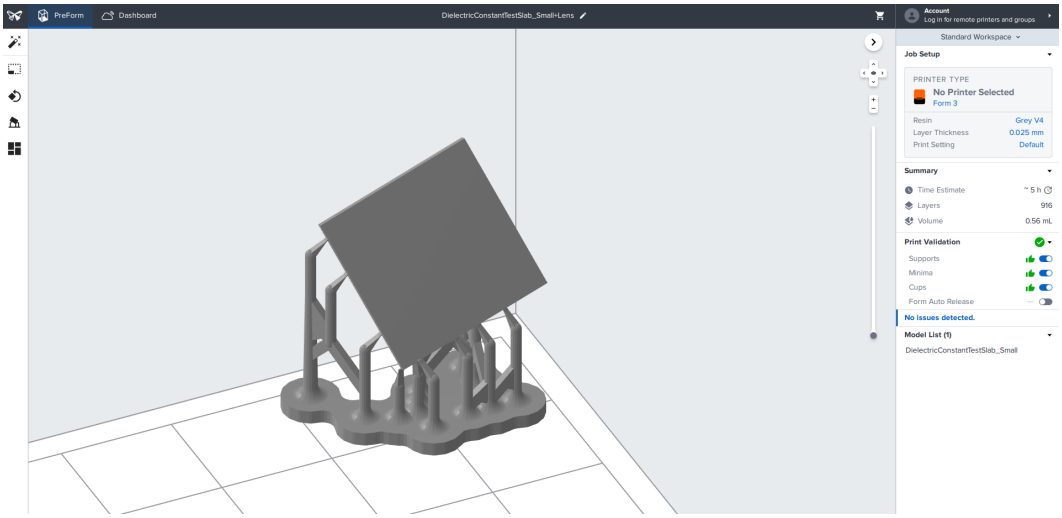

Figure 4.3: Small sample of Grey V4 resin to be printed for characterization of the material.

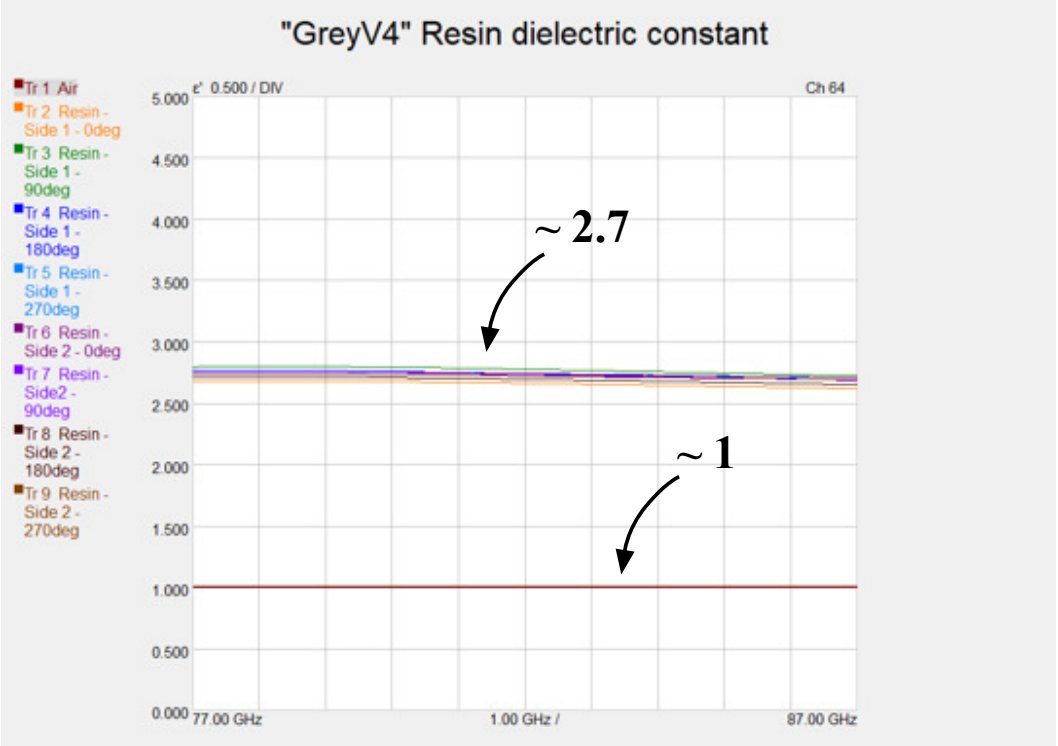

Figure 4.4: Dielectric constant (y axis) vs frequency (x axis) plot of the Grey V4 resin sample, in the Keysight Material Measurement Suite software. The average measured value for the test sample is 2.7.

in Figure 4.3, in which the sample's model is being sliced and supports are added in the PreForm software.

After printing the sample, it was placed in the material characterization setup where it was rotated 90° 4 times per side, for a total of 8 measurements. The obtained data were then introduced into the Keysight Materials Measurement Suite software, which allowed to convert the s2p file into plots of dielectric constant vs frequency. Those plots are displayed in Figure 4.4, where the isolated crimson red line is a reference measure of air, and the other 8 lines represent the data obtained from the performed measurements. The effective dielectric constant of the material was calculated to be approximately 2.7, which came to be the average of all lines. A slight concern when performing this analysis was that the frequency range at which the dielectric constant was measured is not the same as the frequency for which the lens was intended to being fabricated as (3 GHz), but this consideration was later dismissed due to the plots showing a constant behavior and also because of the lack of instrumentation at S-band.

After performing these measurements, the steps explained in chapter 3 were followed, starting with the calculations for the geometry of the lens. Initially, a small variation was applied to Equation 3.1, which is presented below.

$$R = \frac{29.2\lambda_0}{(\theta_{3dB-o})(\varepsilon_T)} \tag{4.1}$$

Where the variables are the same as Equation 3.1, with the added parameter of the tapering efficiency ε_T. An early hypothesis regarding the desired size of the lens included this value as one of the variables in the equation. The logic behind it was that a particular sidelobe level could also be one of the design objectives for the lens, and a particular taper efficiency could be selected according to the expected sidelobes. After simulation testing, this assumption was proved not to be right since the sidelobes were artifacts of

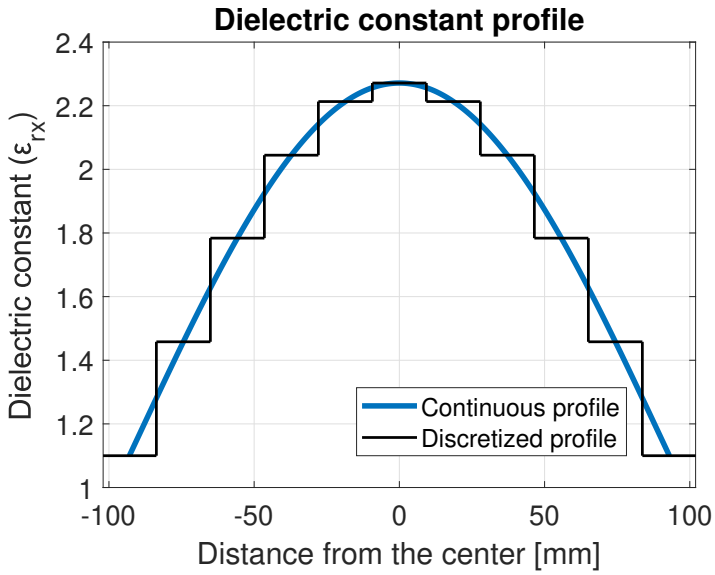

Figure 4.5: Dielectric constant profile of the S-band flat lens.

the illumination level of the lens and the spillover effects. That being said, Equation 4.1 was used to calculate the radius of the lens, for a desired beamwidth of $35°$, a tapering efficiency of 0.85 and a frequency of 3 GHz. This frequency was chosen in accordance with the source antenna, which is a ridged-horn antenna. A diameter of approximately 197 mm, or a radius of 98.5 mm, was calculated. By correcting for the misinterpretation of the tapering efficiency in Equation 4.1, the lens has an actual design output beamwidth of approximately $30°$ instead. Then, Equation 3.2 was used to calculate the focal point. The applied value of θ_{3dB-s} was the E-plane HPBW of the source, in this case $58°$, giving us a focal distance of 177 mm. Since the source antenna is a rectangular ridged horn, it has different beamwidths for each cut, so the H-plane HPBW could have also been used, which would have made the focal point smaller. As a design consideration, following Figure 3.8, the E-plane HPBW was used.

Having both values of lens radius and focal distance, the dielectric constant profile was calculated by applying Equation 3.6, obtaining the one displayed in Figure 4.5. The hexagonal unit cells were then designed with a hexagon side $s = 3.67$ mm, which is approx-

Ring	Dielectric constant	Fractional volume	Hole radius (mm)
1	2.2713	0.1931	1.4667
2	2.2130	0.2194	1.5632
3	2.0445	0.2953	1.8136
4	1.7838	0.4128	2.1442
5	1.4580	0.5595	2.4965
6	1.1000	0.7208	2.8336

Table 4.1: Parameters of the lens for each concentric ring.

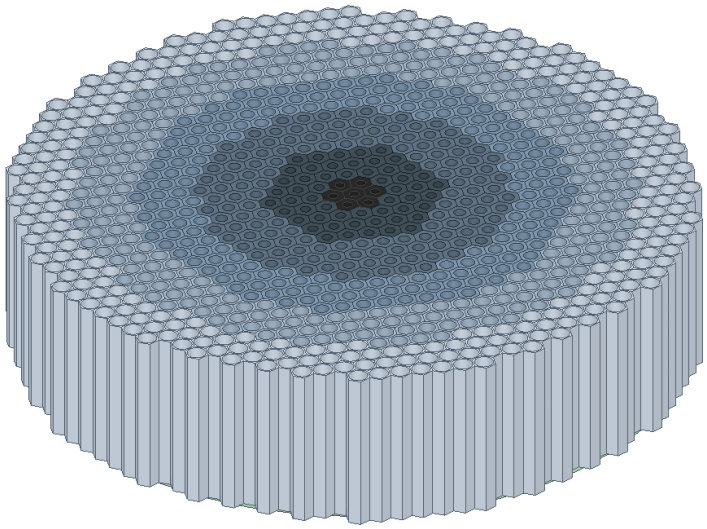

Figure 4.6: Final design of the S-band dielectric lens. The different colors represent different values of dielectric constant.

imately $0.06\lambda_g$, where $\lambda_g = \lambda_0/\sqrt{\varepsilon_r}$, λ_0 being the free-space wavelength, and ε_r being the dielectric constant of the material. The corresponding values of dielectric constant, fractional volume and hole radius are listed in table 4.1.

Following the calculated dielectric constant profile, alongside the respective hole radius of each ring, the unit cells were assembled into the final design of the lens, which is displayed in Figure 4.6.

The source antenna was added to the design to create the simulation setup, which is shown in Figure 4.7, and the lens was placed at its respective focal distance with respect

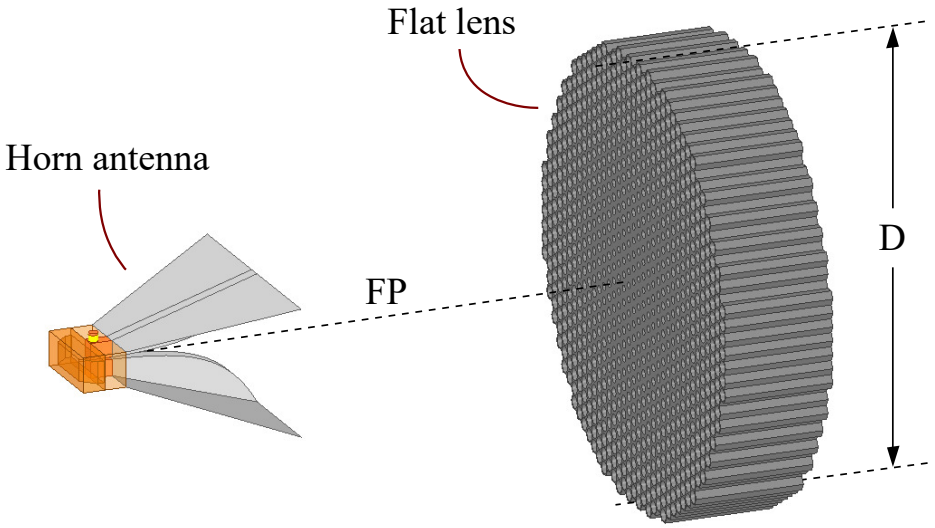

Figure 4.7: Simulation setup of the lens and the source in Ansys HFSS, with the respective focal point (FP) and diameter (D) indicated.

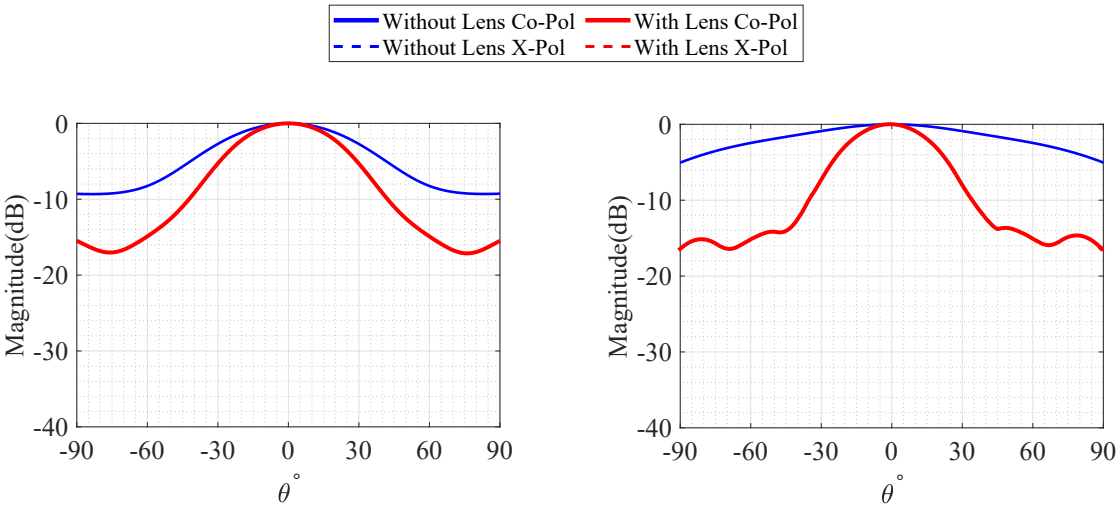

Figure 4.8: Simulated radiation patterns of the (a) E-plane and (b) H-plane of the source with and without the lens.

to the phase center of the source antenna. The phase center was obtained by running a parametrics analysis of the phase difference at multiple points across the direction of propagation, i.e., the Z-axis in Ansys HFSS, and the one with the lowest variation was selected. Figure 4.8 shows the simulated radiation patterns for the E- and H-plane for the source

alone and the source with the lens. The obtained patterns display a clear reduction of the beamwidth for both planes, and no significant crosspolar radiation, i.e., below -40 dB, showing that the lens does not negatively interfere with the fields. There is a small mismatch between the target design beamwidth of $30°$ and the simulated one of approximately $45°$ (for the E-plane) and $37°$ (for the H-plane). This could be attributed to a possible mismatch between the behavior of the lens and an actual radiating aperture antenna (which we approximated as equals), as well as the fact that the lens is not exactly circular, but it has a certain roughness on its edges due to its structure being an assembly of hexagons. This, however, must be compared with the real measurements in the next sections.

4.2 S-band dielectric lens implementation

Due to the large dimensions of the lens, it had to be sliced in four different parts in order for them to fit inside of the 3D printer. The model of one of the four pieces in the PreForm software is shown in Figure 4.9, where it can be seen how large a piece is with respect to the size of the 3D printer platform.

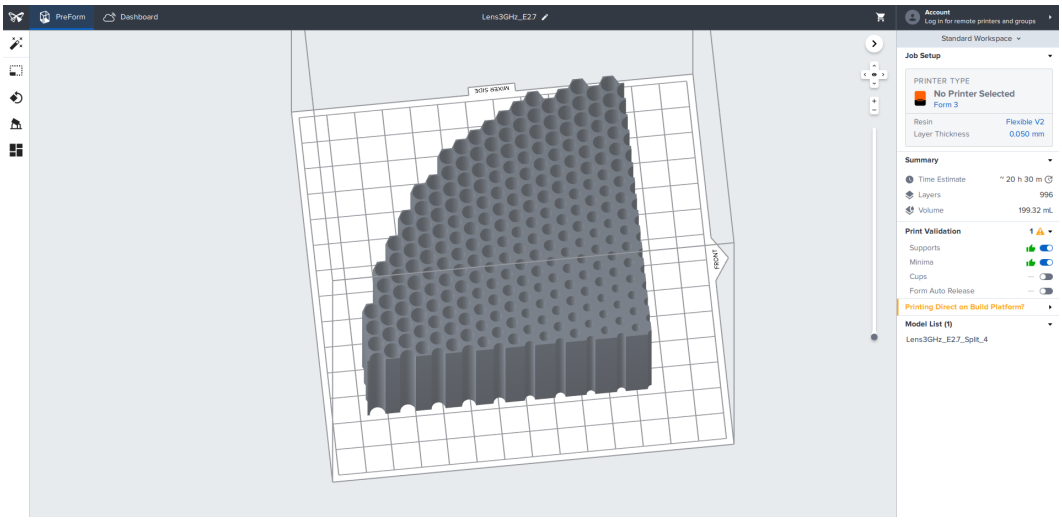

Figure 4.9: Model of one quarter of the lens in PreForm.

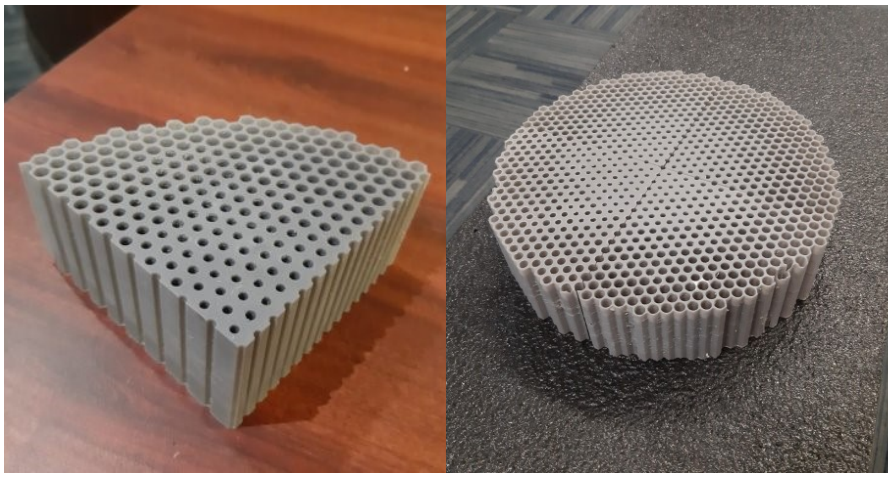

a) b)

Figure 4.10: Fabricated (a) quarter of the lens and (b) fully assembled lens.

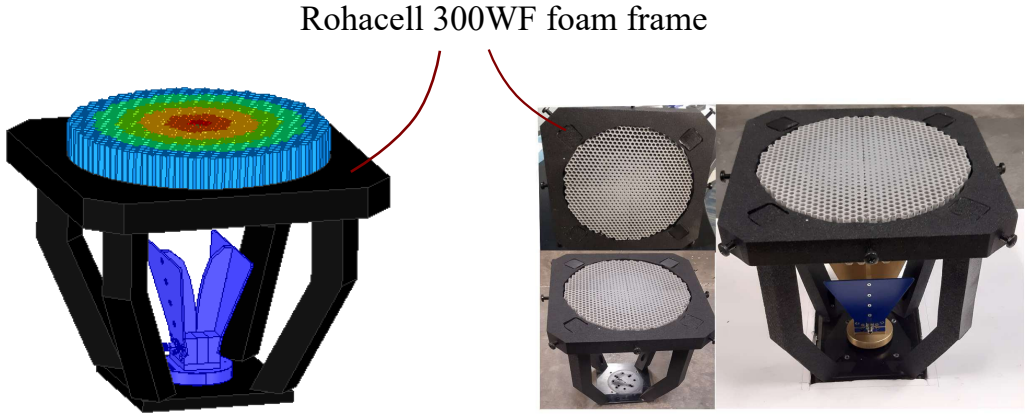

a) b)

Figure 4.11: (a) Model and (b) fabricated frame for the antenna source and the lens.

Figure 4.10-a shows a finalized 3D printed quarter of the lens, that took approximately 20 hours to print. Figure 4.10-b shows the fully assembled lens, where the 4 pieces have been fixed together using epoxy glue. After the lens was fabricated, a frame was designed to hold it in place at the desired focal distance from the source. Figure 4.11-a shows an HFSS model of the frame, and Figure 4.11-b shows the fabricated one. Rohacell 300WF foam was used due to its low dielectric constant ($\varepsilon_r = 1.3$) and loss tangent ($\tan\delta = 0.009$), so

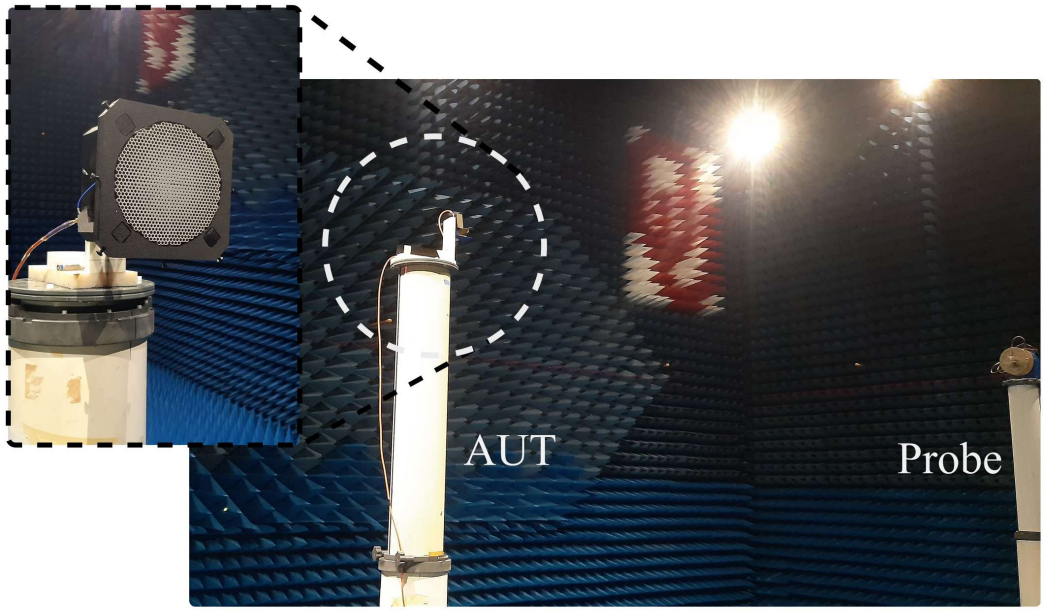

Figure 4.12: Setup of the Antenna Under Test (AUT) with the lens inside of the far-field anechoic chamber.

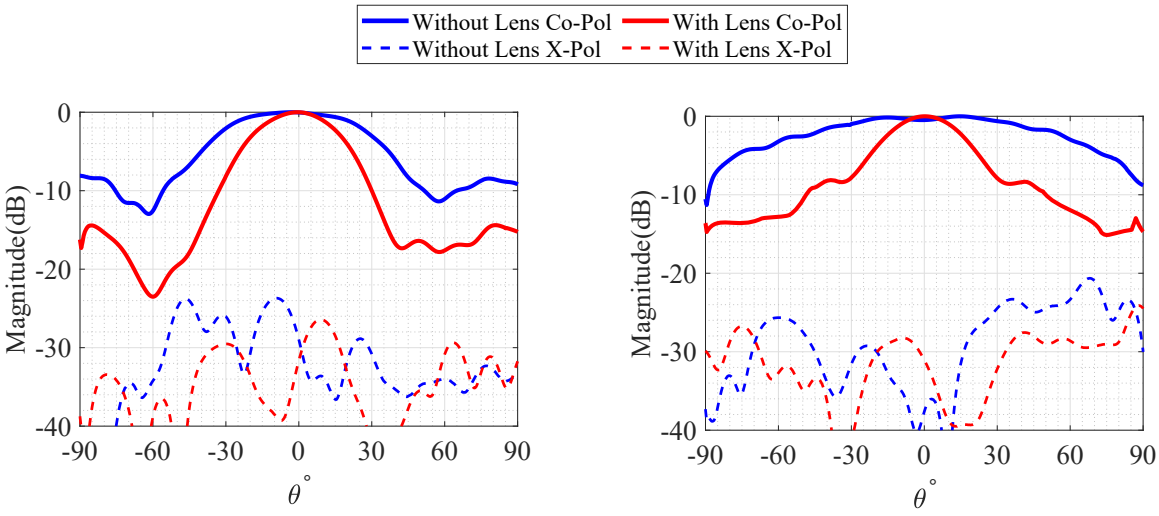

Figure 4.13: Measured radiation patterns of the (a) E-plane and (b) H-plane of the source with and without the lens.

that it does not interfere with the fields radiating to the lens. The lens setup was placed in a far-field anechoic chamber, as displayed in Figure 4.12, and the patterns for 3 GHz were

measured. Figure 4.13 shows these patterns. A beamwidth of around 37° was obtained for the E-plane, and 35° for the H-plane, which are in even better agreement with the theoretical design value than the simulations. There are, however, higher values of crosspol than in the simulated patterns. Looking again at Figure 4.13, we can associated this with the crosspol of the source antenna itself (dashed blue lines).

4.3 Virtual Array design and simulation

A patch antenna array system of 4 transmitting elements and 4 receiving elements was implemented in Ansys HFSS, for a frequency of 3 GHz. This frequency was chosen since each element was created using the HFSS Antenna Toolkit, and the antenna patterns look more symmetrical at lower frequencies. Their individual radiation pattern is shown in Figure 4.14. The setup is shown in Figure 4.15. The Rx element spacing was obtained following Equation 3.17. Additional passive elements were added in every direction to increase the size of the ground plane in order to decrease the effect of diffraction and edge effects. The excitation amplitudes were modified in the receiving array to match Taylor distributions, and the phases of both arrays were modified to achieve beam steering. The simulated patterns of each array were exported to MATLAB and the overall expected two-

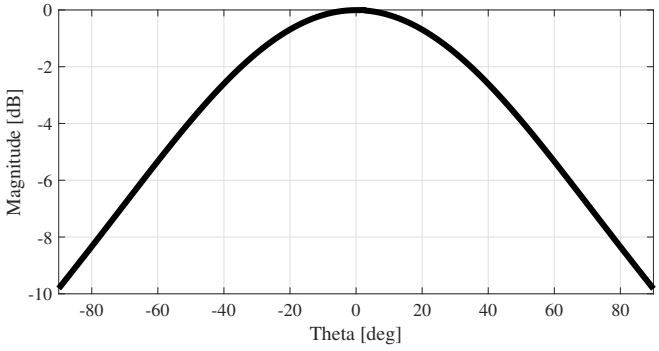

Figure 4.14: Ansys HFSS individual radiation pattern of the antenna element used in the arrays.

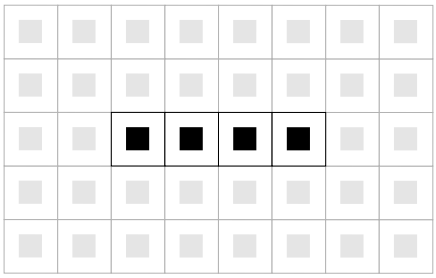

a)

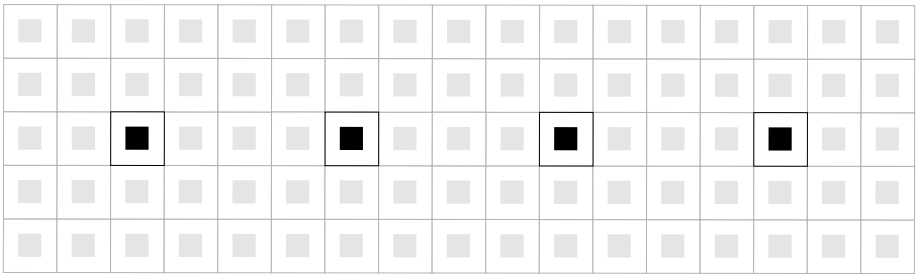

b)

Figure 4.15: Schematic of the (a) transmission and (b) reception arrays simulated in Ansys HFSS. The highlighted antennas are excited, while the rest are just passive elements.

way pattern was calculated as the product of both of them. These patterns are shown in Figure 4.16.

The resulting patterns show the expected behavior, allowing the cancellation of the grating lobes of each reception pattern, while reducing the width of the mainbeam. This is portrayed in the broadside patterns. The original beamwidth obtained when the virtual arrays synthesis method was not applied was 18.4°, while the optimized beamwidth was 6.3° (Figure 4.16-Uniform). This shows a reduction of 12.1°, which is in great agreement with the theoretical curves of Figure 3.16. The usage of Taylor distributions in the reception array also allowed to reduce the sidelobe level, while maintaining great beam steering capabilities. The sidelobe level was improved by the Taylor tapering, but not as much as what was shown in the theoretical patterns. This can be attributed to the effects of the radiation pattern compared with an ideal cosine function. Figure 4.16 shows two examples of

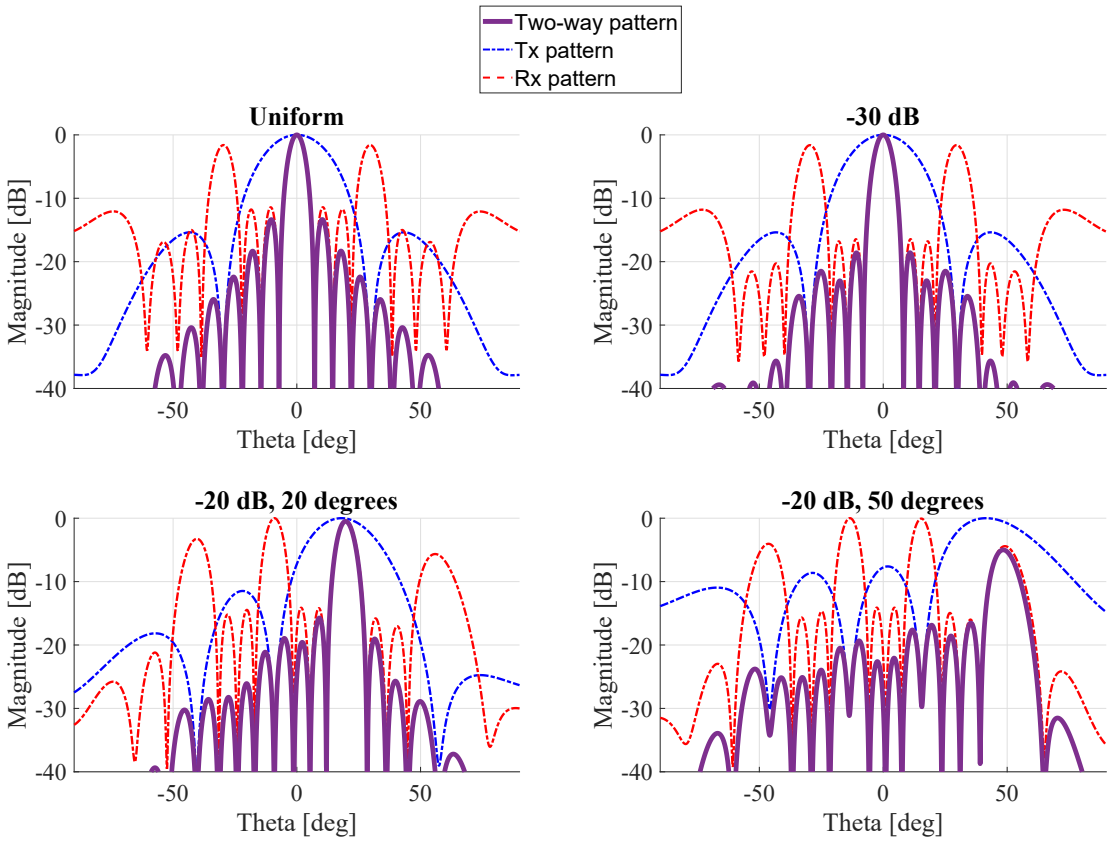

Figure 4.16: Ansys HFSS results of the Virtual Array system for uniform distribution (top left), 30 dB Taylor in the reception array (top right), and beam steering at 20° (bottom left) and 50° (bottom right) with a 20 dB Taylor distribution in the reception array.

beam steering, for 20° and 50°, with no presence of any grating lobe. There are some rather greater sidelobes in the last case (bottom right) due to the nulls that overlap with the grating lobes being slightly higher. This is because of the simulation not having an infinite ground plane. Although the ground plane was extended, as shown in Figure 4.15, thus allowing for deep nulls in low steering angles, it does not seem to be enough for causing that effect on our last plot with 50° in Figure 4.16.

4.4 Virtual Array implementation

Two series-feed four-element patch antenna linear arrays were designed in Ansys HFSS, for the two different given spacings. For ease of fabrication regarding the size of the arrays, a frequency of 10 GHz was chosen. A Rogers 4350B substrate was chosen for this purpose because it can be used in the LPKF ProtoLaser machine in the facilities of the Radars Innovations Lab. This material comes with a dielectric constant of $\varepsilon_r = 3.48$ and a loss tangent of $\tan\delta = 0.0037$. Taking into account the design frequency of the antennas, a thickness of 20 mils was chosen.

After having selected the design frequency and the material to be used, the antennas were designed using the 3D Layout mode of Ansys HFSS, following the steps displayed in Figure 4.17. The process includes designing one single patch antenna to have zero imaginary impedance at the desired frequency, in this case, 10 GHz, then adding bent transmission lines to obtain a 360° phase difference between elements while maintaining the desired spacing between them. Afterwards, multiple elements are assembled, and the input impedance is tuned by a transmission line to obtain only a real component, which is mandatory for the next step. Lastly, a quarter-wave transformer is used to obtain a real 50 ohm input impedance, which will perfectly match with the impedance of the connector. Figures 4.18 and 4.19 show the simulated radiation patterns of both arrays. It is clear that the nulls of one are placed exactly in the same angular positions as the grating lobes of the other one. The models for both arrays were then exported as gerber files into the software of the LPKF machine, which prepares them for fabrication. A picture of the used substrate before being processed by the machine is shown in Figure 4.20. The final fabricated antennas are displayed in Figures 4.21 and 4.22.

The radiation pattern of both antennas were later measured in a near-field anechoic chamber, using the setup displayed in Figure 4.23, with a small Rohacell frame that was

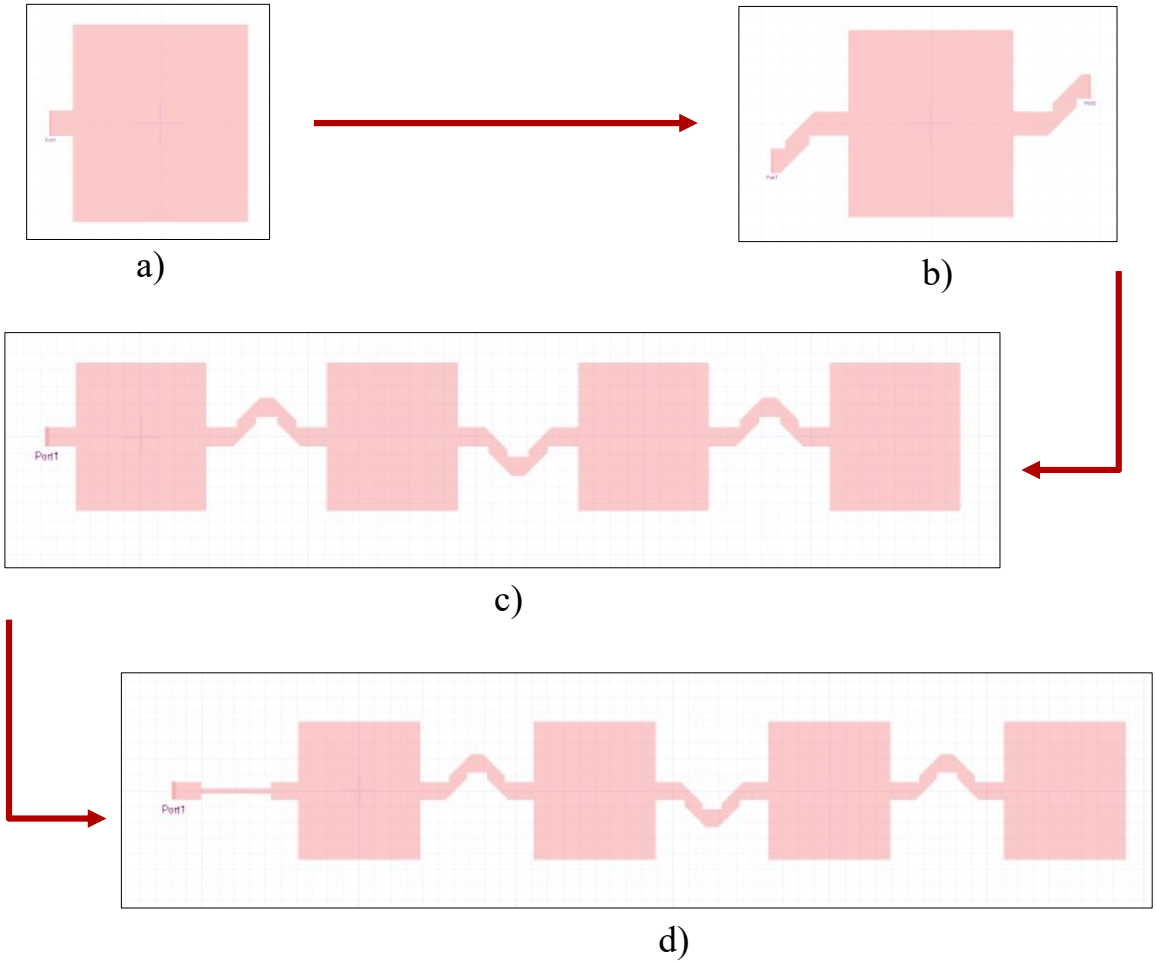

Figure 4.17: Steps for designing a series-feed linear array. (a) A single patch antenna's length and width are tuned to obtain a purely real input impedance at the desired frequency. (b) 50 ohm transmission lines are added at each side of the patch, with a total horizontal length of half-wavelength (or the desired spacing between elements). Mitered bends are added, and their length is tuned to obtain a 360° difference between both ports at the edges of the transmission lines. (c) Multiple elements from step b are assembled together, and a 50 ohm transmission line is added at the beginning of the array. The length of this transmission line is tuned to obtain a purely real input impedance. (d) A quarter-wave transformer is added to convert the input impedance from panel b into 50 ohms. One last 50 ohm transmission line is added after this transformer.

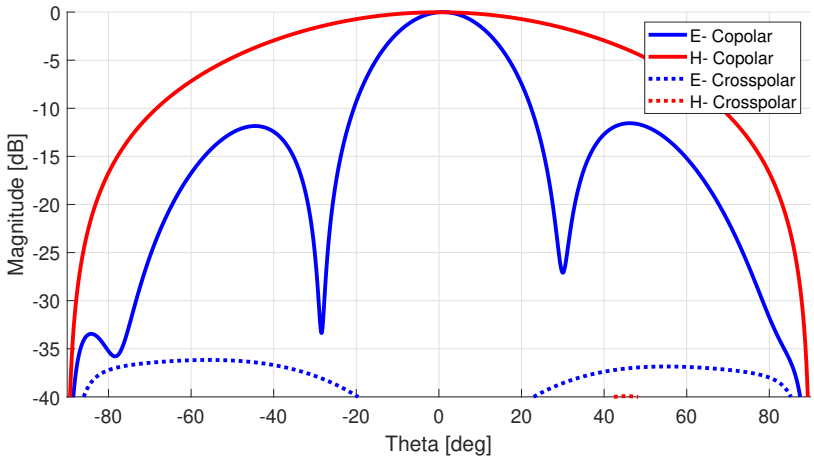

Figure 4.18: Simulated radiation pattern of the series-feed patch antenna array with half-wavelength spacing.

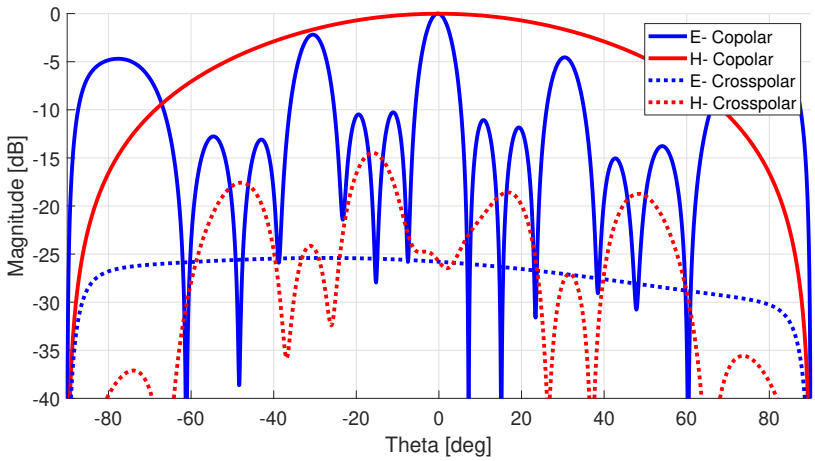

Figure 4.19: Simulated radiation pattern of the series-feed patch antenna array with two-wavelength spacing.

spaced away from the probe by 3.5 inches (about 3 wavelengths at 10 GHz). The far-field patterns were computed using the NSI2000 software, which contains the near-field to far-field transformation equations. The resulting azimuth pattern for the transmission antenna (half-wavelength spacing) is displayed in Figure 4.24, while the one for the reception antenna (two-wavelength spacing) is shown in Figure 4.25, and finally, an overlay of both patterns with the respective two-way pattern is presented in Figure 4.26.

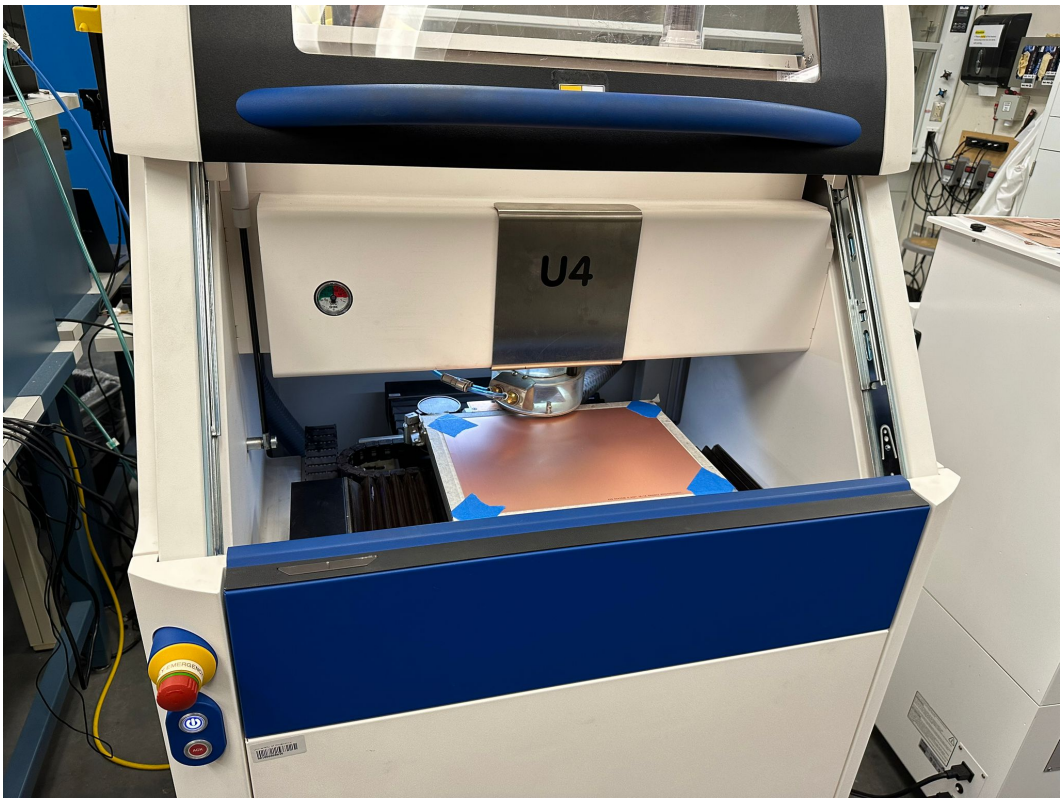

Figure 4.20: Picture of the Rogers 4350B substrate inside of the LPKF ProtoLaser machine. The board has been taped to the surface to secure it during the fabrication process.

It is important to mention that due to performing near-field measurements, the angles in the radiation pattern can only go to around $\pm 70°$. As seen in the two-way pattern, the nulls of transmission and the grating lobes of reception cancel each other out, indicating that the concept of virtual arrays is working. Following Equations 3.14 and 3.16, we can calculate the angular positions of the first null and grating lobe in $\pm 30°$, just like it is shown in the measured results. This setup, however, does not allow to test for some important cases such as scanning out of broadside or applying amplitude tapering to reduce the sidelobe level. This is because the antennas are being fed by only one connector as they are a series-feed array. Therefore, a new setup is proposed for this last analysis, which is displayed in Figure 4.27. The measured elevation cuts for both antennas are used as the pattern of a single element in order to compute the expected array patterns using Equation 2.5. These

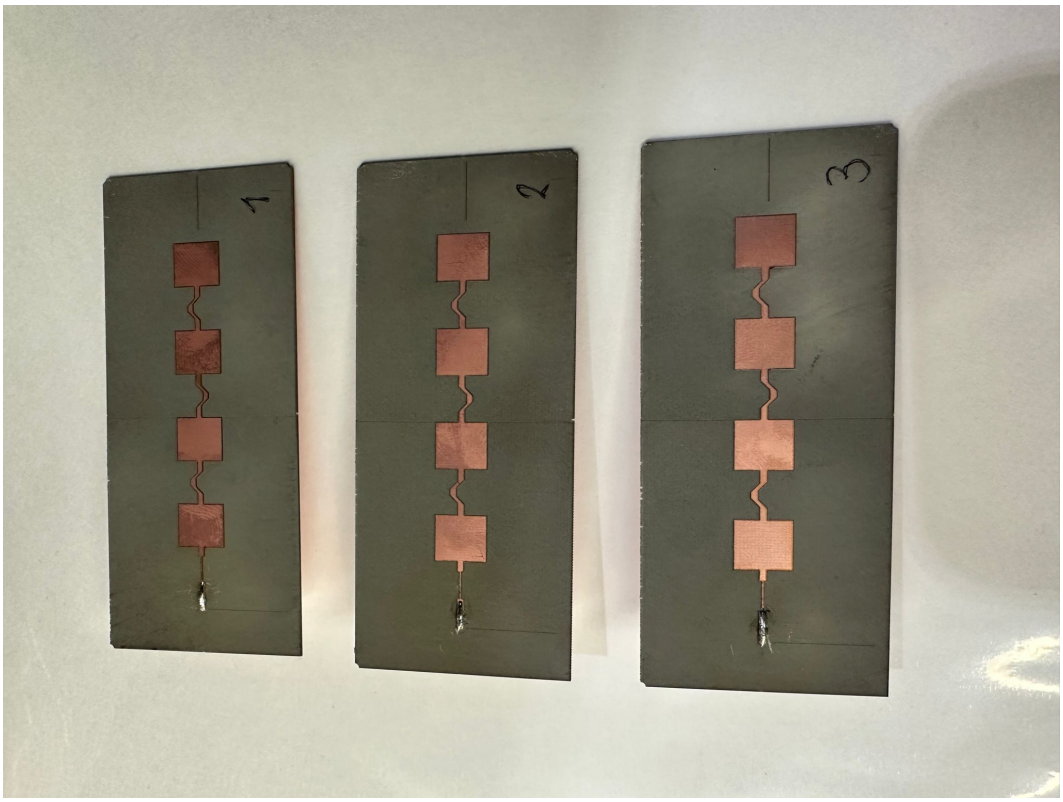

Figure 4.21: Fabricated antenna arrays with half-wavelength spacing. Three arrays were fabricated (labeled 1, 2 and 3) and the one with the best performance was selected.

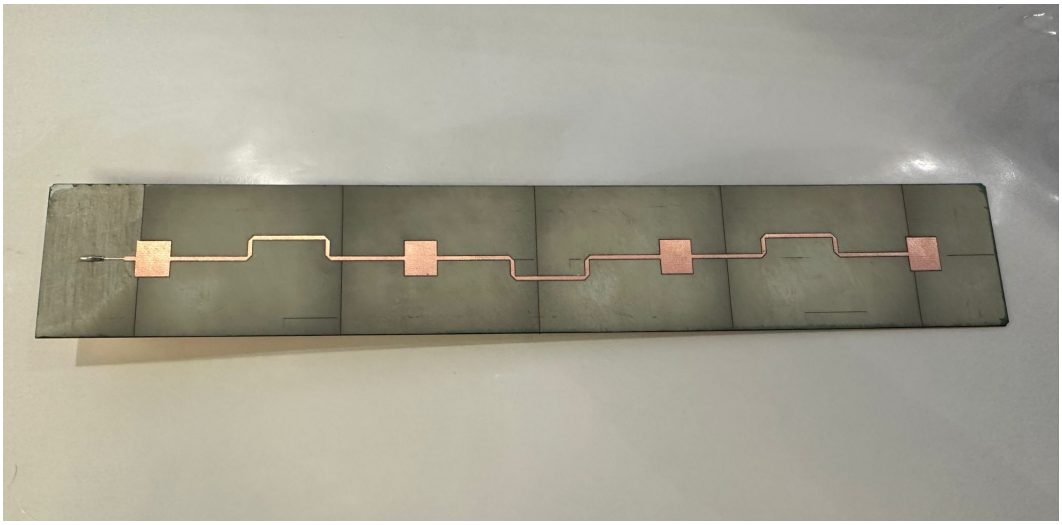

Figure 4.22: Fabricated antenna array with two-wavelength spacing. Only one array was fabricated due to time and lack of material constraints.

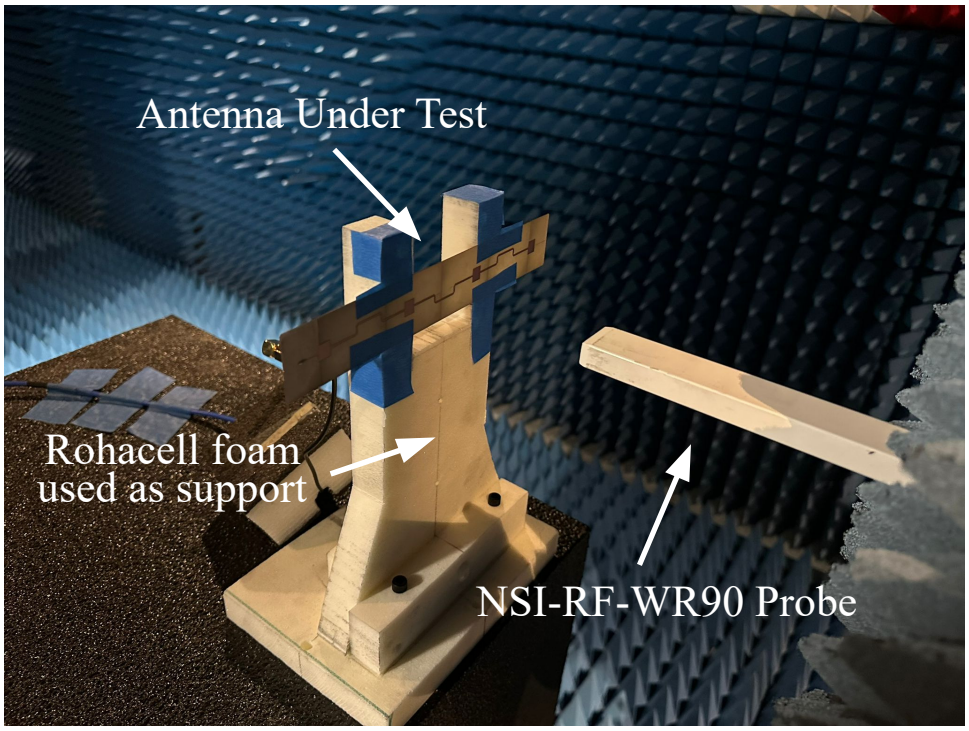

Figure 4.23: Fabricated antenna in the near-field anechoic chamber, with a Rohacell foam support and an NSI-RF-WR90 probe.

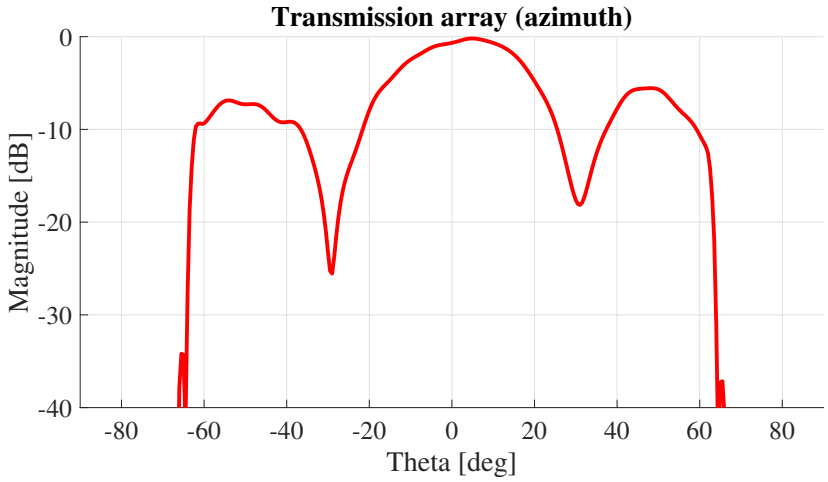

Figure 4.24: Measured azimuth radiation pattern of the transmission antenna array with a half-wavelength spacing. The data is truncated at $\pm 70^{\circ}$ due to the maximum scan window in the chamber and the NSI 2000 software (5'x5').

patterns are portrayed in Figure 4.28, and they are not exactly a cosine function as it was approximated in previous chapters, but they still have similar tendencies. Using these pat-

Figure 4.25: Measured azimuth radiation pattern of the reception antenna array with two-wavelength spacing. The data is truncated at $\pm 70°$ due to the maximum scan window in the chamber and the NSI 2000 software (5'x5').

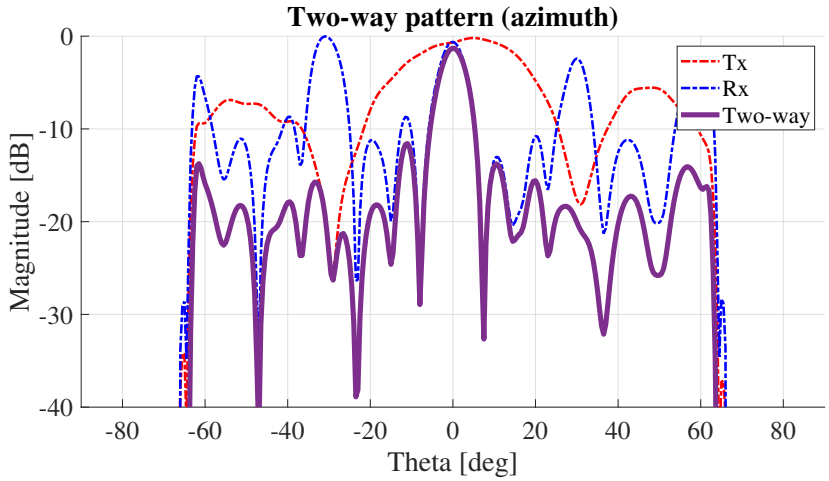

Figure 4.26: Two-way azimuth pattern of the transmission (Tx) and reception (Rx) arrays, calculated and plotted as the overlap between both patterns.

terns, the expected array patterns were obtained using MATLAB, and are shown in Figures 4.29, 4.30 and 4.31. They show a similar behavior to the measured azimuth patterns, but they lean more toward the theoretical ones. We can see the nulls of the transmission array overlapping perfectly with the grating lobes of the reception array, because the individual radiation pattern does not have a large influence in those angular positions as long as it has

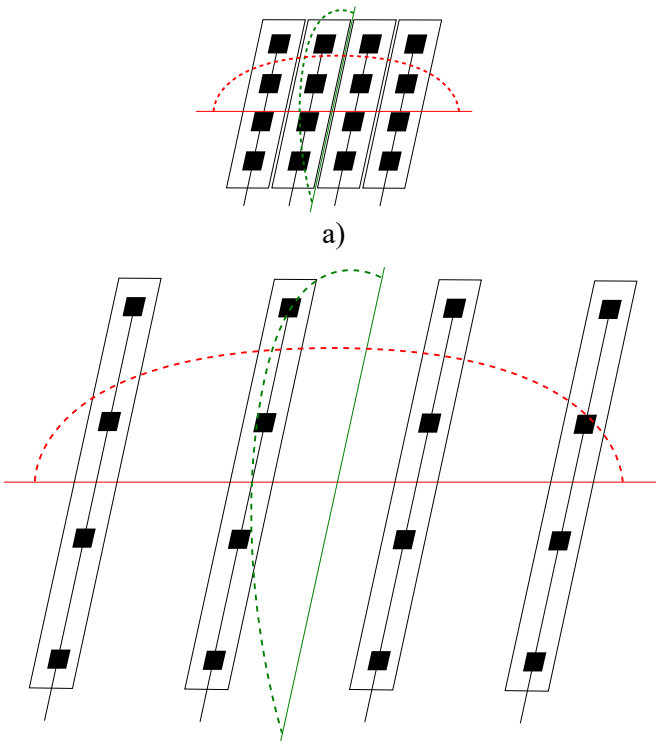

a)

b)

Figure 4.27: Setup to calculate the processed radiation patterns in elevation for (a) half-wavelength spacing and (b) two-wavelength spacing. The azimuth radiation patterns shown were measured for one array alongside the green dashed line axis, whereas the red dashed line indicates that the patterns need to be computed across this axis.

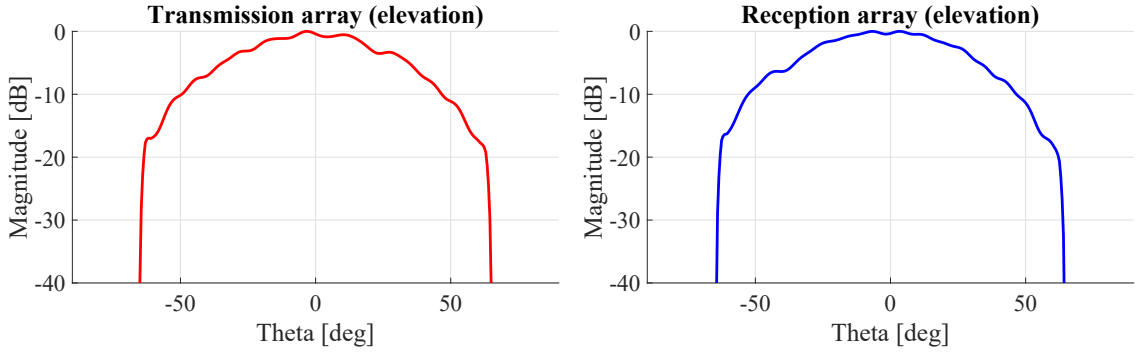

a)

b)

Figure 4.28: Measured elevation radiation pattern of the (a) transmission antenna array with a half-wavelength spacing, and the (b) reception antenna array with two-wavelength spacing.

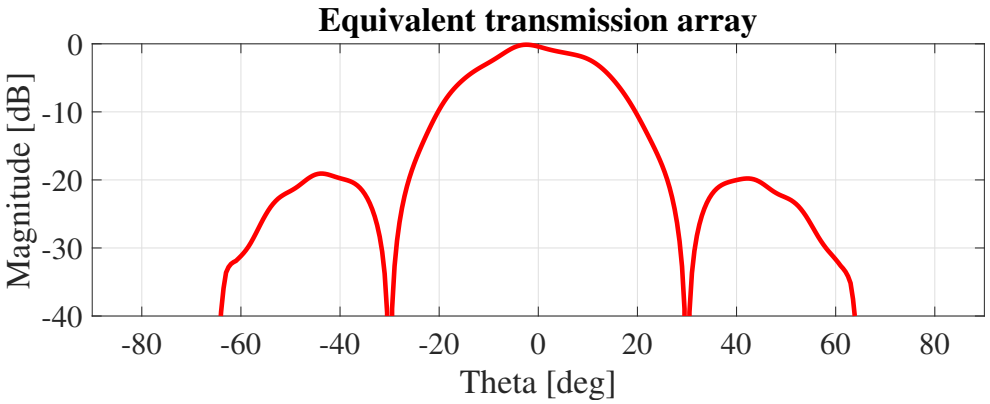

Figure 4.29: Radiation pattern of the equivalent elevation transmission 4-element array with half-wavelength spacing.

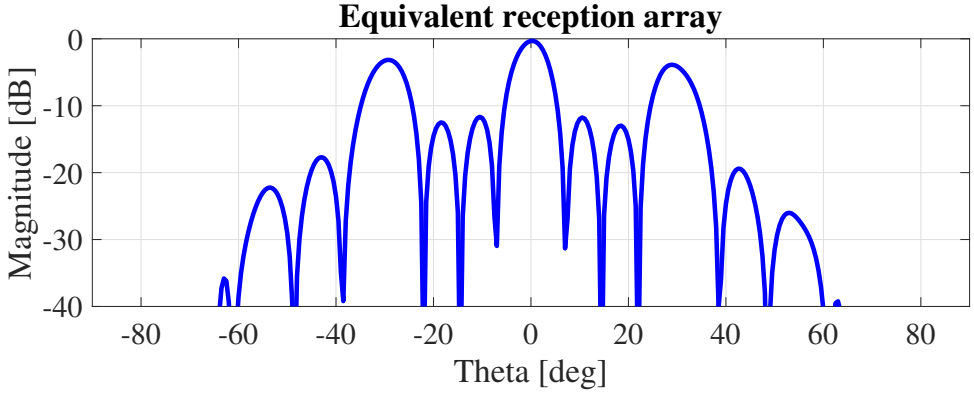

Figure 4.30: Radiation pattern of the equivalent elevation reception 4-element array with two-wavelength spacing.

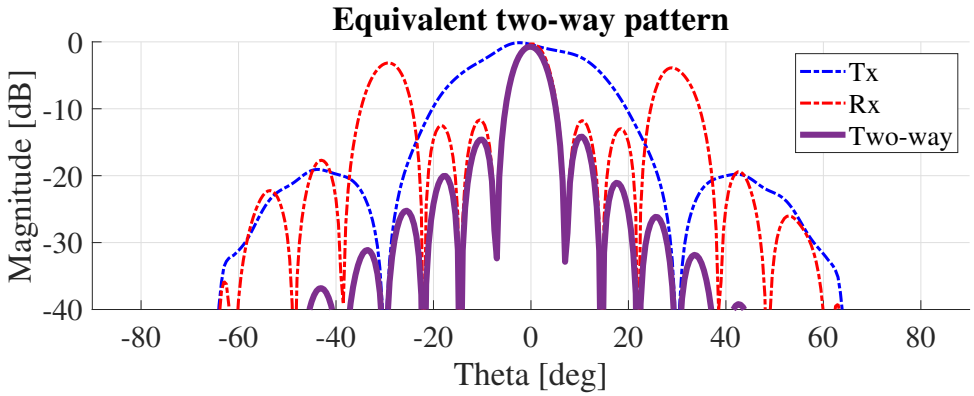

Figure 4.31: Radiation pattern of the equivalent elevation two-way system consisting of transmission (Tx) and reception (Rx).

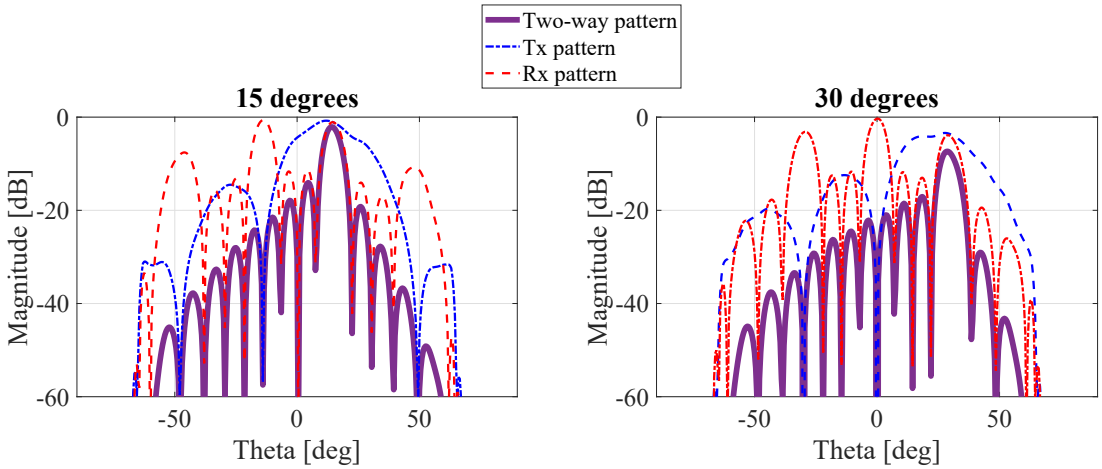

Figure 4.32: Beam steering capabilities of the equivalent elevation two-way system.

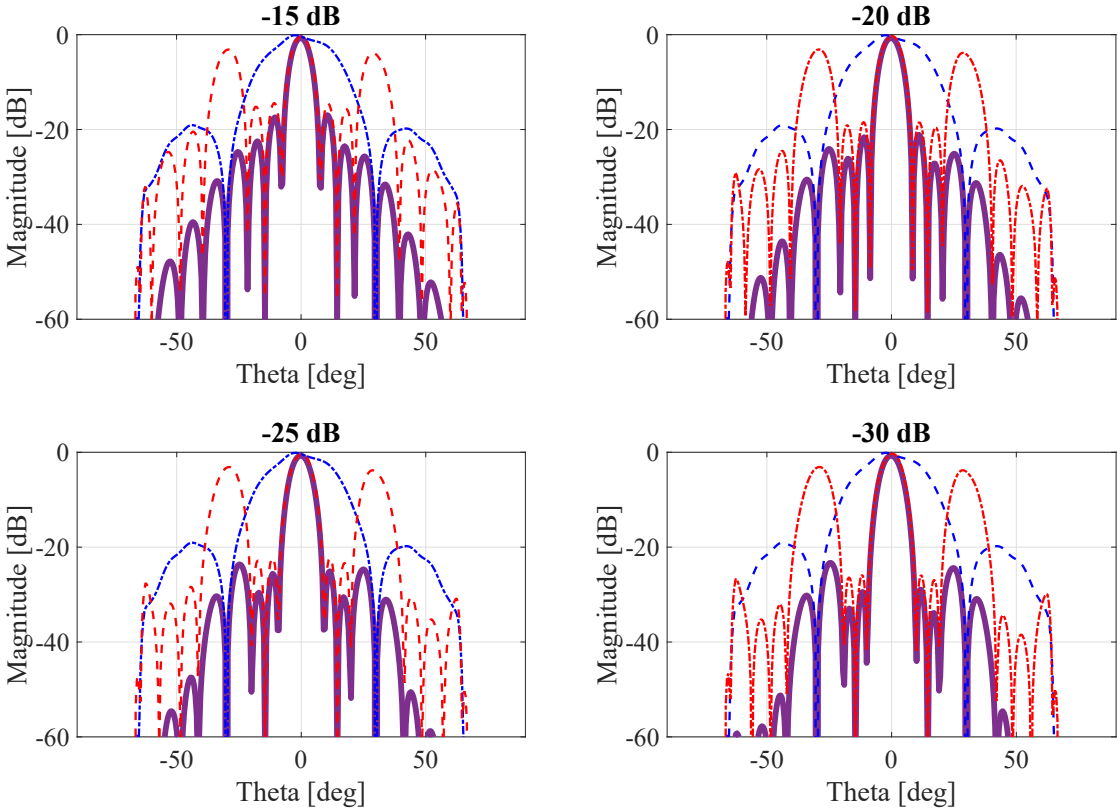

Figure 4.33: Taylor distributions (-15 dB, -20 dB, -25 dB and -30 dB) applied to the amplitudes of the reception array, for the equivalent elevation two-way system.

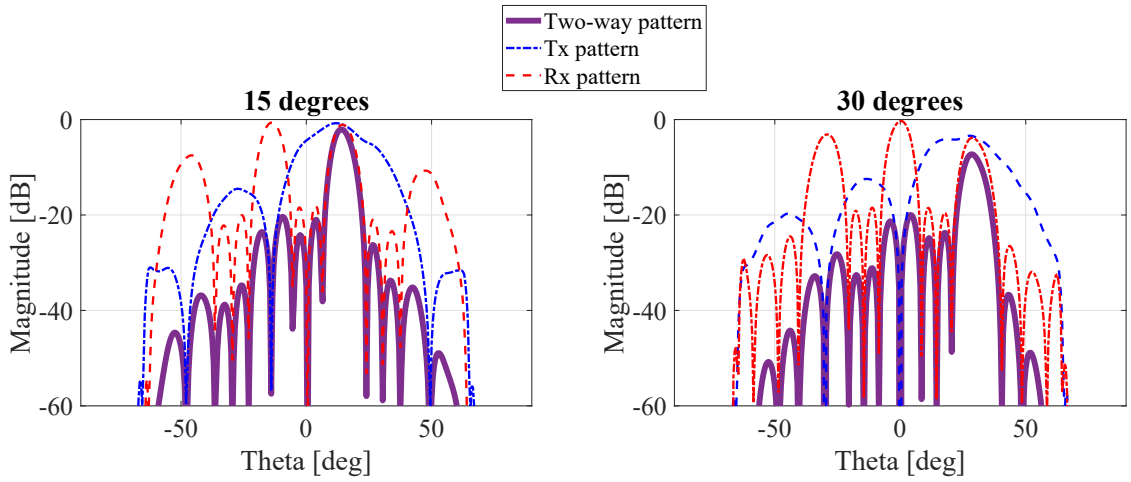

Figure 4.34: Beam steering capabilities of the equivalent elevation two-way system, with a -20 dB Taylor tapering in reception.

a wide beam, such as the cosine function that was used in earlier chapters.

Now, the most important part of this last section is applying beam steering and amplitude tapering, which are shown in Figures 4.32 (steering), 4.33 (tapering) and 4.34 (both). We can see that both concepts were achieved, but the beam steering was slightly limited to lower angles. This is because the measured radiation patterns in elevation are limited to about $\pm 60°$, so we see nulls there. This limits our scanning capabilities when processing the data because of the pattern roll-off at higher angles. Nonetheless, there should not be a problem in a real array with a wide pattern that does not suddenly stop at a certain angle below $90°$.

Lastly, in order to appropriately test beam steering and amplitude tapering without having to process the measured data, a more refined 16x1 S-band probe-fed patch antenna array was used, with its own TR module with 8-bit phase-shifters and attenuators. A picture of this array in the anechoic chamber is displayed in figure 4.35. Only four elements were used at a time, following the diagram shown in figure 4.36, where the highlighted elements were the used ones. Just like with the X-band arrays, the transmission array has a spacing of half-wavelength, and the reception array has a spacing of two wavelengths. Due to the

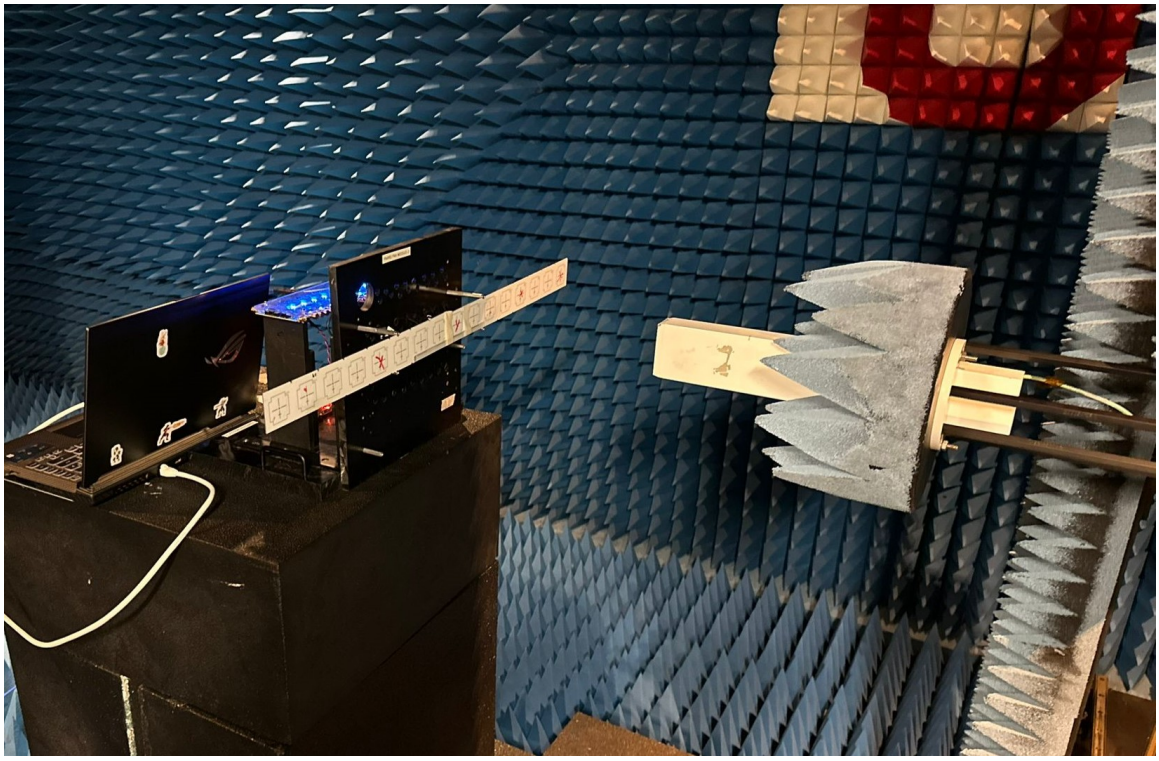

Figure 4.35: 16x1 S-band patch antenna array placed in the near-field anechoic chamber for measurements.

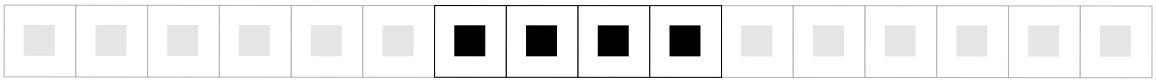

a)

b)

Figure 4.36: Setup of the 16x1 S-band antenna array, where the highlighted elements are the only ones that were excited for measuring (a) transmission with a spacing of half-wavelength and (b) reception with a spacing of two wavelengths.

presence of the TR module, beam steering and amplitude tapering were also tested, but also taking into account that the maximum scanning angles of the near-field chamber are $\pm 60°$. The measured patterns were then overlapped to obtain two-way patterns, and they are dis-

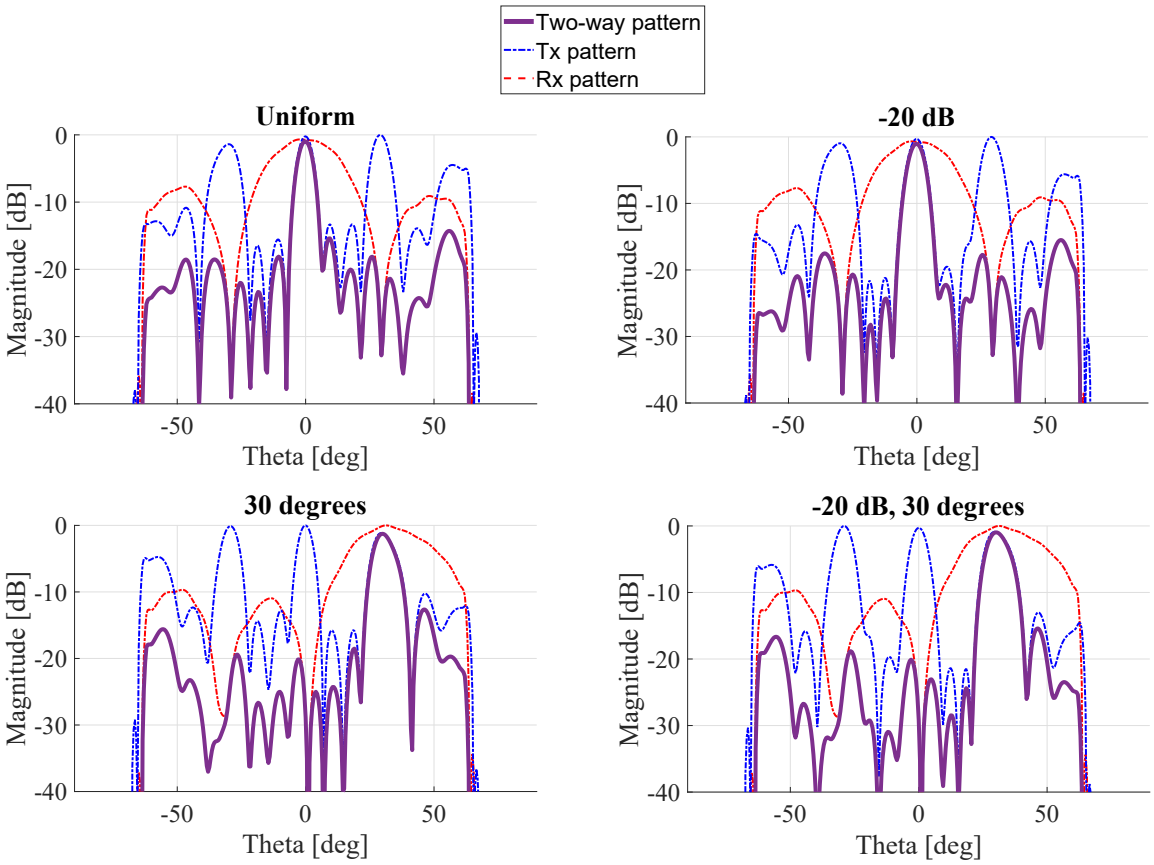

Figure 4.37: Measured results of the two-way system by using the S-band antenna array with two configurations for transmission and reception. The plots show uniform distribution (top left), 20 dB Taylor in the reception array (top right), beam steering at 30° (bottom left), and both beam steering (30°) and Taylor tapering (-20 dB) in the reception array (bottom right).

played in figure 4.37. The first two-way pattern shows the cancellation of the grating lobes and the nulls in a similar way as the measured X-band pattern in figure 4.26. Then, the top right plot shows a -20 dB Taylor distribution on the reception array, effectively reducing the sidelobes next to the main beam (around $\pm 10°$). The other sidelobes are not greatly reduced because the tapering does not reduce the grating lobes, but only the sidelobes in-between them. Next, the bottom left plot shows beam steering at 30 degrees, and even though there are some big sidelobes at high angles, the two grating lobes are perfectly cancelled by the nulls at $-30°$ and $0°$. Lastly, the bottom right plot shows the same beam steering angle, but

with a -20 dB Taylor distribution in the reception array. Just like with the second plot, the sidelobes next to the main beam are greatly reduced without compromising the periodical cancellation of grating lobes in our virtual array.

4.5 Summary

An S-band dielectric lens was designed and fabricated using additive manufacturing. The dielectric constant of the resin that was used for the 3D printing was first measured using a small printed rectangular slab in a material characterization setup using a Vector Network Analyzer. The derived equations from earlier chapters were used and a first model was obtained and simulated in Ansys HFSS. The lens was then printed in 4 sections and put together using epoxy glue. A frame was also fabricated and the whole setup was measured in a far-field anechoic chamber. The simulations showed a reduced beamwidth of 45° for the E-plane and 37° for the H-plane. The measured patterns, on the other hand, show closer values in beamwidth to the theoretical design value of 30°, with 37° in the E-plane and 35° in the H-plane.

Two X-band series-feed linear antenna arrays were also fabricated to verify the virtual array concept. Both arrays were designed with different values of spacing, and were fabricated using a Rogers 4350B substrate in an LPKF ProtoLaser machine. The arrays were then measured in a near-field anechoic chamber, and their respective far-field patterns were computed using a near-field to far-field transformation. The obtained two-way pattern enabled the cancellation of grating lobes in reception with the nulls in transmission, located in $\pm 30^\circ$. Furthermore, in order to have results that account for beam steering and amplitude tapering, the measured elevation patterns were used after being processed to create the expected patterns of a larger array. This allowed the achievement of patterns similar to those of the theoretical ones explained in earlier chapters, testing for amplitude tapering

that allowed a sidelobe level down to -30 dB, and beam steering up to 30 degrees, limited by the data truncation caused in the near-field measurements. Lastly, a 16x1 S-band array was used for final measurements due to having an 8-channel TR module with phase shifters and attenuators that allowed to test two-way patterns steering out of broadside and having reduced sidelobes with amplitude tapering. Uniform and -20 dB Taylor distributions were tested, steering at 0 and 30 degrees, achieving the desired cancellation of the grating lobes in all four cases, supporting the theoretical procedure for designing virtual arrays.

Chapter 5

Epilogue

5.1 Conclusion

A study of beamforming techniques that aim to obtain a narrow beamwidth in antenna systems has been provided, in order to facilitate the development of high frequency systems in which complexity, power density, cost and number of active components are challenging limitations. Particularly, out of those beamforming techniques, dielectric lenses and virtual arrays are explored. Wide research has been performed for both cases, but some limitations are identified, such as a lack of a methodical design procedure, as well as restrictions in the beam steering capabilities of the systems. Based on this, methodical procedures are proposed and developed for the design process of dielectric lenses and virtual arrays that allow the reduction of the antenna beamwidth.

Basic antenna concepts are provided, in order to facilitate the understanding of the proposed work. The radiation pattern of an antenna system, as well as all of its respective parameters are presented and discussed. Fundamentals of antenna arrays are also examined and illustrated, emphasizing on how their patterns change according to the way in which the elements are organized. In addition, refraction theory and basic optical lenses are reviewed, aiming to correlate these concepts with lenses in microwave frequencies.

For dielectric lenses, the dimensions are given by approximating the surface as a radi-

ating aperture antenna, the focal point is calculated based on how much radiation is desired in the dielectric surface, a dielectric constant profile equation is derived to compensate for phase shifts, and hexagonal unit cells are proposed for the assembly of a large cylindrical lens with concentric rings of different permittivities. Another derived equation for the dielectric constant profile is also discussed, which can allow to design conformal lenses with different shapes, improving the equation in the literature that is only used for purely flat lenses. Furthermore, for virtual arrays, the equations for nulls and grating lobes in antenna arrays are compared in order to obtain one single equation that allows for acquiring a two-way radiation pattern with the narrowest achievable beamwidth. Beam steering and Taylor tapering are also analyzed and discussed, achieving both of them without the presence of grating lobes, which results in an improvement from the cases in the literature that only work on broadside or certain scanning angles. A tradeoff analysis is performed for both dielectric lenses and virtual arrays.

An S-band dielectric lens was designed, simulated and fabricated using additive manufacturing, with a commercial resin 3D printer. It was printed in 4 sections, assembled together using epoxy glue, and then put in place with the respective source using a frame. The setup was measured in a far-field anechoic chamber, and the resulting patterns show the expected reduction of the antenna beamwidth, with 37° in the E-plane and 35° in the H-plane, compared with the theoretical design value of 30°. Additionally, a pair of X-band antenna arrays with different element spacing were designed, simulated and fabricated, in order to test the virtual array concept. They were then measured in a near-field anechoic chamber, and the obtained two-way pattern shows the expected cancellation of grating lobes and nulls, located in $\pm 30^\circ$. Moreover, the elevation planes of the measured patterns were processed to obtain an equivalent larger virtual array and test the scanning and tapering capabilities, supporting sidelobes down to -30 dB and scanning up to 30 degrees, limited due to the truncation of the data in the near-field chamber. Lastly, an S-band 16x1

array with its own TR module with phase shifters and attenuators was used for measuring two-way patterns with beam steering at 30 degrees and -20 dB Taylor tapering, allowing to fully support with actual measurements that both concepts work when following the provided design procedure.

These findings have significant implications for high-frequency antenna systems, in which increasing the number of active elements is not cost-effective. The development of design procedures and considerations to narrow the beamwidth of antennas opens up the possibility to fabricate good performing systems that are also affordable.

In conclusion, this thesis establishes the potential of these two beamwidth reduction techniques, and gives a detailed design procedure for them, successfully achieving the initial objectives.

5.2 Future Work

Regarding future work, one of the main objectives would be to perform measurements in higher frequencies with both techniques, as their main use is to make mm-Wave systems more feasible and affordable. Currently, S-band and X-band systems were designed, and more precise 3D printers and circuit board fabrication devices would be required to obtain a dielectric lens and an antenna array suitable for a high frequency.

Regarding Chapter 3, simulations of different lenses at different frequencies would be useful to test how accurate the approximation of the lens being similar to a circular aperture antenna is, and in which cases the obtained beamwidth drifts off from the expected one too much.

When considering Chapter 4, designing a conformal lens that is not flat across all of its surface could serve in testing how the derived equation for the dielectric constant profile might be more flexible than the one used in the literature. The presented equation in this

work calculates the phase shifts in every point of the lens, so lenses with arbitrary shapes according to the application can be achieved instead of only flat ones, thus broadening the scope of this technique.

References

[1] D. Liu, U. Pfeiffer, B. Gaucher, and J. Grzyb, *Advanced Millimeter-Wave Technologies*. Wiley, 2009.

[2] X. Gao, L. Dai, and A. M. Sayeed, "Low RF-complexity technologies to enable millimeter-wave MIMO with large antenna array for 5G wireless communications," *IEEE Communications Magazine*, vol. 56, no. 4, pp. 211–217, 2018.

[3] M. H. Mazaheri, S. Ameli, A. Abedi, and O. Abari, "A millimeter wave network for billions of things," in *Proceedings of the ACM Special Interest Group on Data Communication*, ser. SIGCOMM '19. New York, NY, USA: Association for Computing Machinery, 2019, p. 174–186. [Online]. Available: https://doi.org/10.1145/3341302.3342068

[4] A. A. Baba, R. M. Hashmi, K. P. Esselle, M. Attygalle, and D. Borg, "A millimeter-wave antenna system for wideband 2-D beam steering," *IEEE Transactions on Antennas and Propagation*, vol. 68, no. 5, pp. 3453–3464, 2020.

[5] E. Carpentieri, U. F. D'Elia, E. De Stefano, L. Di Guida, and R. Vitiello, "Millimeter-wave phased-array antennas," in *2008 IEEE Radar Conference*, 2008, pp. 1–5.

[6] C. A. Balanis, *Antenna Theory: Analysis and Design*, 3rd ed. Wiley, 2005.

[7] R. E. Rinehart, *Radar for Meteorologists*, 2nd ed. Rinehart Pub, 1997.

[8] D. M. Tuan, Y. Cheon, Y. Aoki, and Y. Kim, "Performance comparison of millimeter-wave communications system with different antenna beamwidth," in *2016 10th European Conference on Antennas and Propagation (EuCAP)*, 2016, pp. 1–5.

[9] H. He, S. Zhang, Y. Zeng, and R. Zhang, "Joint altitude and beamwidth optimization for UAV-enabled multiuser communications," *IEEE Communications Letters*, vol. 22, no. 2, pp. 344–347, 2018.

[10] S. Rao, "MIMO radar," 2017. [Online]. Available: https://www.ti.com/lit/pdf/swra554

[11] M. Richards, "Virtual arrays part 2: Virtual arrays and coarrays," *Tech. Memo*, 2019.

[12] K. Sultan, H. Abdullah, E. Abdallah, and H. El-Hennawy, "MOM/GA-based virtual array for radar systems," *Sensors*, vol. 20, no. 3, 2020. [Online]. Available: https://www.mdpi.com/1424-8220/20/3/713

[13] D. Ramaccia, F. Scattone, F. Bilotti, and A. Toscano, "Broadband compact horn antennas by using EPS-ENZ metamaterial lens," *IEEE Transactions on Antennas and Propagation*, vol. 61, no. 6, pp. 2929–2937, 2013.

[14] X. Chen and Y. Ge, "Enhancing the radiation performance of a pyramidal horn antenna by loading a subwavelength metasurface," *IEEE Access*, vol. 5, pp. 20 164–20 170, 2017.

[15] M. K. T. Al-Nuaimi, W. Hong, and Y. Zhang, "Design of high-directivity compact-size conical horn lens antenna," *IEEE Antennas and Wireless Propagation Letters*, vol. 13, pp. 467–470, 2014.

[16] R. J. Bauerle, R. Schrimpf, E. Gyorko, and J. Henderson, "The use of a dielectric lens to improve the efficiency of a dual-polarized quad-ridge horn from 5 to 15 GHz," *IEEE Transactions on Antennas and Propagation*, vol. 57, no. 6, pp. 1822–1825, 2009.

[17] A. S. Turk and A. K. Keskin, "Partially dielectric-loaded ridged horn antenna design for ultrawideband gain and radiation performance enhancement," *IEEE antennas and wireless propagation letters*, vol. 11, pp. 921–924, 2012.

[18] T. McManus, R. Mittra, and C. Pelletti, "A comparative study of flat and profiled lenses," in *Proceedings of the 2012 IEEE International Symposium on Antennas and Propagation*, 2012, pp. 1–2.

[19] S. Zhang, R. K. Arya, S. Pandey, Y. Vardaxoglou, W. Whittow, and R. Mittra, "3D-printed planar graded index lenses," *IET Microwaves, Antennas & Propagation*, vol. 10, no. 13, pp. 1411–1419, 2016.

[20] J.-M. Poyanco, F. Pizarro, and E. Rajo-Iglesias, "Cost-effective wideband dielectric planar lens antenna for millimeter wave applications," *Scientific Reports*, vol. 12, no. 1, p. 4204, 2022.

[21] S. Zhang, R. K. Arya, W. G. Whittow, D. Cadman, R. Mittra, and J. Vardaxoglou, "Ultra-wideband flat metamaterial grin lenses assisted with additive manufacturing technique," *IEEE Transactions on Antennas and Propagation*, vol. 69, no. 7, pp. 3788–3799, 2020.

[22] M. Imbert, A. Papió, F. De Flaviis, L. Jofre, and J. Romeu, "Design and performance evaluation of a dielectric flat lens antenna for millimeter-wave applications," *IEEE Antennas and Wireless Propagation Letters*, vol. 14, pp. 342–345, 2014.

[23] Y. Liu, Z. Nie, and Q. H. Liu, "Reducing the number of elements in a linear antenna array by the matrix pencil method," *IEEE Transactions on Antennas and Propagation*, vol. 56, no. 9, pp. 2955–2962, 2008.

[24] H. Shen and B. Wang, "An effective method for synthesizing multiple-pattern linear arrays with a reduced number of antenna elements," *IEEE Transactions on Antennas and Propagation*, vol. 65, no. 5, pp. 2358–2366, 2017.

[25] H. Kikuchi, Y. Hobara, and T. Ushio, "Compressive sensing to reduce the number of elements in a linear antenna array with a phased array weather radar," *IEEE Transactions on Geoscience and Remote Sensing*, vol. 60, pp. 1–10, 2022.

[26] W. Zhang, L. Li, and F. Li, "Reducing the number of elements in linear and planar antenna arrays with sparseness constrained optimization," *IEEE Transactions on Antennas and Propagation*, vol. 59, no. 8, pp. 3106–3111, 2011.

[27] A. H. Dorrah and G. V. Eleftheriades, "Peripherally excited phased arrays: Beam steering with reduced number of antenna elements," in *2019 IEEE Canadian Conference of Electrical and Computer Engineering (CCECE)*, 2019, pp. 1–4.

[28] R. Mailloux, *Phased Array Antenna Handbook*, 3rd ed., 2017.

[29] K.-C. Huang and Z. Wang, "Millimeter-wave circular polarized beam-steering antenna array for gigabit wireless communications," *IEEE Transactions on Antennas and Propagation*, vol. 54, no. 2, pp. 743–746, 2006.

[30] Y. Wang, H. Wang, and G. Yang, "Design of dipole beam-steering antenna array for 5G handset applications," in *2016 Progress in Electromagnetic Research Symposium (PIERS)*, 2016, pp. 2450–2453.

[31] Z. Li, E. Ahmed, A. M. Eltawil, and B. A. Cetiner, "A beam-steering reconfigurable antenna for WLAN applications," *IEEE Transactions on Antennas and Propagation*, vol. 63, no. 1, pp. 24–32, 2015.

[32] A. J. Fenn, D. H. Temme, W. P. Delaney, and W. E. Courtney, "The development of phased-array radar technology," *Lincoln laboratory journal*, vol. 12, no. 2, pp. 321–340, 2000.

[33] T. C. Cheston and J. Frank, "Phased array radar antennas," *Radar Handbook*, pp. 7–1, 1990.

[34] M. Danielsen and R. Jorgensen, "Frequency scanning microstrip antennas," *IEEE Transactions on Antennas and Propagation*, vol. 27, no. 2, pp. 146–150, 1979.

[35] Y. Yusuf and X. Gong, "A low-cost patch antenna phased array with analog beam steering using mutual coupling and reactive loading," *IEEE Antennas and Wireless Propagation Letters*, vol. 7, pp. 81–84, 2008.

[36] E. Topak, J. Hasch, C. Wagner, and T. Zwick, "A novel millimeter-wave dual-fed phased array for beam steering," *IEEE Transactions on Microwave Theory and Techniques*, vol. 61, no. 8, pp. 3140–3147, 2013.

[37] R. Xu and Z. N. Chen, "A compact beamsteering metasurface lens array antenna with low-cost phased array," *IEEE Transactions on Antennas and Propagation*, vol. 69, no. 4, pp. 1992–2002, 2021.

[38] "IEEE recommended practice for antenna measurements," *IEEE Std 149-2021 (Revision of IEEE Std 149-1977)*, pp. 1–207, 2022.

[39] E. G. Plaza, G. Leon, S. Loredo, and L. F. Herran, "Calculating the phase center of an antenna: A simple experimental method based on linear near-field measurements. [measurements corner]," *IEEE Antennas and Propagation Magazine*, vol. 59, no. 5, pp. 130–175, 2017.

[40] R. Kingslake and J. R. Barry, *Lens Design Fundamentals*, 2nd ed. Elsevier, 2010.

[41] S. S. Jehangir, Z. Qamar, N. Aboserwal, and J. L. Salazar-Cerreno, "Application of the mixing theory in the design of a high-performance dielectric substrate for microwave and mm-wave systems," *IEEE Access*, vol. 8, pp. 180 855–180 868, 2020.

[42] M. I. Skolnik, *Introduction to Radar Systems*, 3rd ed. McGraw-Hill Education, 2002.

[43] T. Taylor, "Design of line-source antennas for narrow beamwidth and low side lobes," *Transactions of the IRE Professional Group on Antennas and Propagation*, vol. 3, no. 1, pp. 16–28, 1955.